University of Alberta

The effects of core-mantle gravitational coupling on the rotational dynamics of Mercury

by

Martin James Veasey

A thesis submitted to the Faculty of Graduate Studies and Research
in partial fulfillment of the requirements for the degree of

Master of Science
in
Geophysics

Department of Physics

Fall 2010
Edmonton, Alberta

Examining Committee

Dr. Mathieu Dumberry

Department of Physics

Dr. Moritz Heimpel

Department of Physics

Dr. Jeffrey Kavanaugh

Department of Earth and Atmospheric Sciences

Dr. Bruce Sutherland

Departments of Physics and Earth and Atmospheric Sciences

Abstract

As Mercury orbits the Sun, solar induced gravitational torques give rise to a planetary libration, which has been detected by Earth based radar speckle patterns. The amplitude of this libration suggests that only the mantle participates in the libration motion, thereby indicating a decoupling with the core. This is seen as proof that the outermost part of the core is fluid. While the planet undergoes its 88 day period libration, the axes of minimum moment of inertia of the mantle and solid core, if present, become misaligned, leading to a gravitational torque between the two. This initiates a free-mode of axial oscillation between the inner core and mantle. For a large gravitational torque, the free-mode period approaches the period of the libration forcing, and should participate in the planet's libration response. The goal of this work is to determine whether Mercury's observed librations can be used to place constraints on the size of its inner core. We model Mercury with three concentric layers, including a solid mantle and fluid and solid cores. By numerically solving the governing set of coupled differential equations, perturbations in Mercury's rotation rate are simulated for a range of interior structures. The model response is compared to spin rate observations. For models where the free-mode interferes with the libration signature, a marginally better fit between model response and observations is obtained, compared to models which exhibit the libration signature alone. We show that the best fit to observations occurs for an inertial ratio $\frac{B_m - A_m}{C_m} = (2.19 \pm 0.04) \times 10^{-4}$ and inner core radius $r_s > 500$ km.

Acknowledgements

I would like to thank Sarah Derr for her administrative help over the past two years. I would also like to acknowledge Wladek Rudzinski for the excellent job he conducted as a TA coordinator. Many thanks to Dan Laycock and Laurence Koot for their continual input during my studies. Last, but certainly not least, I am indebted to Mathieu Dumberry, who has surpassed my every expectation of a supervisor. His time, knowledge and unwavering support have been invaluable during my time in Canada.

Contents

List of Figures

List of Tables

Chapter 1

Introduction

Mercury is one of the least explored planets in our Solar System. Limited information regarding the planet's dynamics and bulk physical properties have been provided by Earth-based telescopic measurements and the Mariner 10 satellite mission of 1975. The close proximity of Mercury to the Sun however, makes the planet difficult to observe from Earth, and as a consequence Earth-based measurements are sparse, both in terms of planetary coverage and in quantity. The data retrieved from the Mariner 10 mission also lacks the precision that could be gained by using newer measuring techniques. An increase in precision is imperative for placing tighter constraints on physical models of the planet, and will inevitably improve the accuracy of simulations of internal physical processes. The deficit of comprehensive data pertaining to Mercury's composition, internal structure and magnetic and gravitational fields has been the driving impetus behind the launch of two new satellite missions, MESSENGER, an acronym for MErcury Surface, Space ENvironment, GEochemistry, Ranging (Solomon *et al.* 2001) and BepiColombo (Anselmi & Scoon, 2001), which are projected to be in full orbit in the years 2011 and

2020 respectively. The aim is to gather data on a range of properties with increased precision and coverage, whilst capturing any time dependence that these properties exhibit. Ultimately, the data will be used in an attempt to unlock the key to terrestrial planet evolution.

Despite the currently limited information that is available, much can still be learned using the existing data. It is critical to work out models that make testable predictions in order to prepare the necessary framework in which to discuss the measurements the two future missions will be able to carry out. This research in particular assesses the role of inner core-mantle gravitational coupling on Mercury's rotation rate. There has been little discussion regarding this type of coupling on Mercury, and it is most often neglected due to its seemingly negligible effect on rotation rate (e.g. Peale *et al.* 2002). The present work provides a more extensive investigation into the role of inner core-mantle gravitational coupling for a range of models of Mercury's interior structure. We also discuss how Mercury's spin rate is affected by its shape and the magnitude of the gravitational couple, along with how the comparison of simulated spin rates with observations might be able to provide constraints on inner core radius. The size of Mercury's inner core radius in particular is a vital prerequisite for determining Mercury's evolutionary history as well as its dynamo generation mechanism.

1.1 Observations of Mercury's Shape and Composition

Mercury has the highest uncompressed density[1] (5300 kg m^{-3}) of the ter-

[1]Reduced to standard conditions of room temperature 20°C and pressure 0.1 GPa.

restrial planets (Spohn *et al.* 2001). In comparison, the uncompressed density of Earth is 4400 kg m^{-3} and Mars, 3800 kg m^{-3}. Mercury's high density suggests that the planet has a large core with an iron-silicate ratio that is more than twice that of the other terrestrials (Wasson, 1988; Balogh & Giampieri). This comparatively anomalous value has led to a host of theories regarding the mechanism of the planet's accretion (e.g. Weidenschilling, 1978; Cameron, 1985; Fegley & Cameron, 1987; Benz *et al.* 1988; Wetherill, 1988), since it almost certainly differs from that of the other terrestrial planets.

Mercury is not perfectly spherical in shape, and consists of a broad range of perturbations from spherical symmetry. Although these perturbations are manifest in the physical shape of the planet, they are also related to a spectrum of perturbations in the gravity field which can be described by a set of surface spherical harmonic functions with coefficients C_{lm}, S_{lm}. The degree l and order m describe how the gravitational potential depends on latitude and longitude, while the magnitude of C_{lm}, S_{lm} describe the relative magnitude of each coefficient in the description of the global gravitational potential. It should be noted that the perturbations in the shape of the planet do not necessarily coincide with the perturbations in the gravity field, except in the circumstance of hydrostatic equilibrium. The largest perturbation in Mercury's shape from spherical symmetry is caused by the planet's oblateness (e.g. flattening in a pole to pole sense), which is related to the gravitational coefficient $C_{20} = (-6 \pm 2) \times 10^{-5}$ (Anderson *et al.* 1987). This value is larger than the suggested value of $C_{20} \approx 10^{-6}$ for a body in hydrostatic equilibrium at its current rotation period of 58.65 Earth days (Balogh & Giampieri, 2002). It has been hypothesised that the excess equatorial bulge must be either a remnant of a more rapid rotation rate in the past (Lambeck & Pullan, 1980), a consequence of non-hydrostatic processes such as internal mantle convection

(past or present), or a finite strength lithosphere (Zuber *et al.* 2007).

The second largest perturbation in Mercury's shape is from equatorial flattening (i.e. the equatorial cross-section is elliptical), which gives the planet a slightly prolate shape. The amount to which the planet is prolate is related to the gravitational coefficient $C_{22} = (1.0 \pm 0.5) \times 10^{-5}$ (Anderson *et al.* 1996). The non-zero C_{22} value is the consequence of a difference in the two planetary equatorial moments of inertia, which has a significant effect on the planet's rotation and internal coupling, as discussed in section 1.2. A summary of Mercury's bulk properties can be found in table 1.1.

Table 1.1: Bulk properties of Mercury

Parameter	Value
Mass[1] (kg)	3.302×10^{23}
Mean radius[1] (km)	2440
Mean uncompressed density[2] (kg m^{-3})	5300
Mean density[1] (kg m^{-3})	5427
Surface gravity[1] (m s^{-2})	3.70
C_{20}	$-(6 \pm 2) \times 10^{-5}$
C_{22}	$(1.0 \pm 0.5) \times 10^{-5}$

[1]From Yoder (1995); [2]From Wood *et al.* (1981).

1.1.1 Composition of the Mantle and Crust

Compared to Earth, there is currently little knowledge on the structure of Mercury's mantle and crust. Furthermore, there are no observed surface features with typical length scales associated with a subsurface chemical or rheological discontinuity that hint at the existence of a low density crust (Solomon *et al.* 1981). An average crustal thickness of 200 ± 100 km has been calculated by comparing Mercury's equatorial ellipticity to the gravitational coefficient

C_{22} and assuming that the equatorial ellipticity is isostatically compensated due to Airy isostasy (Anderson *et al.* 1996). However, since it is expected that pressure, density and elastic moduli vary little through the crust and mantle (Spohn *et al.* 2001), the mantle and crust are often collectively referred to as a 'thin, silicate shell' with a typical silicate density of approximately 3300 kg m^{-3}. Mercury's high iron-silicate ratio demands that the silicate shell is thin ($\sim 400 - 700$ km), since a large, dense core is necessary to match observations of the mean density of the planet.

1.1.2 Core structure and Composition

Mercury's core is relatively large in comparison with the cores of the other terrestrials. Schubert *et al.* (1988) have used the mean density to deduce that a metallic core with a radius of at least $0.7R$ must persist, possibly even as large as $0.75R$ (Siegfried & Solomon, 1974) where R is the planetary radius. The chemical composition of the core is known to consist predominantly of iron, since no other heavy element has a cosmic abundance that can account for Mercury's observed density (Zuber *et al.* 2007). Recent observations of Mercury's spin rate suggest that the outermost part of the core is fluid (Margot *et al.* 2007)(see section 1.2.1), though this does not discount the possible existence of a solid inner core. The presence of an inner core is expected as a result of planetary cooling, and is predicted by thermal history models (e.g. Solomon, 1976). Observations of uniformly distributed lobate scarps on Mercury's surface, interpreted as surface features of large scale faults, are thought to be a consequence of planetary contraction (Strom *et al.* 1975; Watters *et al.* 1998), with estimates of radial decrease around 3 km (Solomon *et al.* 2008;

Heimpel & Kabin, 2008). This observed contraction is consistent with the presence of a solid inner core, due to the density increase upon solidification. The presently on-going solidification of an inner core is also consistent with Mercury's global magnetic field, which is suspected to be dynamo generated (see section 1.1.4). Inner core freezing provides a mechanism for compositional buoyancy, where the segregation of chemical compounds occur by virtue of differences in melting temperature (Loper & Roberts, 1981). The energy release from the effects of buoyancy and also the release of latent heat both promote convection and dynamo action.

The present work examines Mercury's core structure. Our aims are twofold: (a) To assess the role of a solid inner core on Mercury's spin rate, and, in the affirmation of (a), (b) to extend the groundbreaking work of Margot *et al.* (2007) by determining whether the size of Mercury's solid inner core can be constrained using observations of its spin rate.

1.1.3 The Role of Sulphur in the Core

The detection of a fluid core by Margot *et al.* (2007) contradicts older thermal evolution models, which show that if Mercury's core were composed of pure iron, it should have fully solidified since the planet's accretion (Stevenson *et al.* 1983; Schubert *et al.* 1988). However, it has been postulated by Stevenson *et al.* (1983) that the presence of sulphur could enable a fluid core to be retained by depressing the melting point of iron-sulphur mixtures. Other volatile elements (those that vaporise at relatively low temperatures) such as oxygen and silicon may also be present, but are unable to depress the melting temperatures of metallic alloys (Williams & Jeanloz, 1990). The addition of sulphur in a metallic mixture also has the effect of reducing the density of the

mixture. These combined effects make core sulphur concentration a controlling factor over the radii of both the outer and inner cores. A high sulphur concentration, for example, would imply a larger radius of the whole core (due to its reduced density) and delay the precipitation of a solid inner core. In contrast, a negligible quantity of sulphur would imply a smaller core, and a quicker attainment of a fully solidified core. The state of the core can therefore be used to determine the presence of volatile elements in the core, which is conducive to modelling Mercury's evolution. Other studies have considered the concentration of sulphur by looking at heliocentric gradients (changes with respect to distance from the Sun) in the composition of condensed matter in the Solar System. The conclusion of such studies show that if Mercury condensed from the solar nebula at its present location, it should be depleted in volatile elements including sulphur (Lewis 1972; 1988; Chapman 1988; Goettel 1988). This result is in conflict with Margot *et al'*s (2007) detection of a fluid core, suggesting that Mercury did not accrete *in situ*, but at another location in the solar nebula where a greater abundance of volatile elements exist (e.g. Wetherill, 1988). A catastrophic collision may have then removed a substantial part of Mercury's mantle and forced the planet to migrate to its current position (Benz *et al.* 1988).

1.1.4 Reconciling a Fluid Core with Mercury's Magnetic Field

Between 1974 and 1975, the Mariner 10 space mission detected an unequivocally intrinsic global magnetic field (Ness *et al.* 1974). More recent data coming from the Messenger mission flybys have revealed that the field is predominantly dipolar, with a tilt between 5° and 12° from the rotation axis

(Anderson *et al.* 2008). Although the magnetic moment of the field is roughly 1.1% of Earth's, it is strong enough to create a magnetosphere that acts to deflect the solar wind. The sparseness of magnetic field data has resulted in little knowledge of the temporal and spatial variation of the field, which is necessary to determine the field's origin. One possibility is that the field may be the result of magnetisation of Mercury's crust, either by a presently active dynamo, or from a frozen-in remnant magnetisation. Any remnant magnetisation may have been acquired through either an internal dynamo that has since decayed, or an external source such as the primordial Sun or solar nebula (Schubert *et al.* 1988). The latter is unlikely since the high temperatures that are expected at this early stage of evolution are least favourable for magnetisation. The dipolar structure of the global field favours a dynamo origin, but observations of temporal changes in the field are required to confirm that this is the case. Although the Messenger flybys have detected no change in the planetary dipole from the Mariner 10 data, core dynamo simulations have shown that secular variation is likely to occur over timescales of centuries rather than decades if a stagnant layer at the top of the outer core is present (Anderson *et al.* 2008). Thus, long term observations of the magnetic field will be likely necessary if temporal changes are to be found. If Mercury's magnetic field is internally generated, constraining the size of the inner core will confirm whether the dynamo exhibits a 'thick' or 'thin' shell regime. The shell size refers to the thickness of the fluid outer core relative to the total core radius and hence gives an indication of the size of the inner core. Modelling of the two regimes (eg. Christensen, 2006; Stanley *et al.* 2005; Heimpel *et al.* 2005) has shown different field structures at the core-mantle boundary (CMB), so magnetic field observations from Messenger and BepiColombo should also be able to distinguish between 'thick' and 'thin' shell scenarios (Zuber *et al.*

2007). This will possibly provide a future alternative method to constraining Mercury's inner core radius.

1.2 Mercury's Rotational Characteristics

Mercury is the closest planet to the Sun, and follows an eccentric orbit with eccentricity $e = 0.206$. It takes approximately 88 Earth days for Mercury to orbit the Sun, during which it rotates about its spin axis once every 59 Earth days. The rotation period is exactly 2/3 the orbital period, resulting in a 3:2 spin-orbit resonance (Pettengill & Dyce, 1965), which is thought to be a consequence of tidal dissipation (Colombo, 1965; Colombo & Shapiro, 1966; Goldreich & Peale, 1966). Mercury's obliquity (the angle between the equatorial and orbital planes) is very close to 0° (Peale, 1988), so all motion, at least on timescales similar to the rotation period, is restricted to the orbital plane. A summary of rotation and orbital characteristics is given in table 1.2.

Table 1.2: Rotation and orbital parameters

Parameter	Value
Sidereal orbital period (Earth days)	87.97
Sidereal rotation period (Earth days)	58.65
Orbital eccentricity	0.206
Obliquity (arc minutes)[1]	2.1 ± 0.1
Semi-major axis (km)	5.79×10^7
Perihelion (km)	4.60×10^7

Data from Yoder (1995) except [1]from Margot *et al.* (2007).

1.2.1 The Origin of Mercury's Libration

Mercury's prolate figure has a significant effect on the way the planet rotates about its spin axis. As Mercury orbits the Sun, solar induced gravitational torques, which reverse as Mercury rotates, act on the planet's equatorial structure (figure 1.1). The effect of the torque changes the spin-angular momentum balance about Mercury's spin axis and causes small perturbations in its resonant spin rate. Since the spin axis is approximately perpendicular to the ecliptic, the perturbation acts almost entirely in the planet's axial plane and is observed as a change in Mercurian Length of Day (LOD). Such oscillations in longitude are known as *physical* (or *forced*) librations, and have a period that coincides with Mercury's orbital period of approximately 88 days.

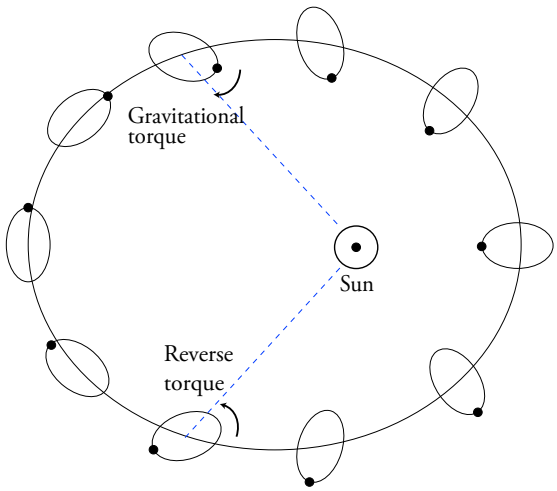

Figure 1.1: Top down view of Mercury's counter-clockwise orbit around the Sun at successive time intervals. Dots mark one end of the axis of minimum moment of inertia. The gravitational torque acts to realign this axis with the Mercury-Sun line. Adapted from Zuber *et al.* (2007).

The amplitude of libration ϕ_0 is defined as the maximum deviation of the axis of minimum moment of inertia from that which would result from uniform

rotation, and can be written as (e.g. Peale, 1972)

$$\phi_0 = \frac{3}{2}\left(\frac{B-A}{C}\right)\left(1 - 11e^2 + \frac{959}{48}e^4 + \dots\right) \tag{1.1}$$

where A < B are the principal equatorial moments of inertia and C is the polar moment of inertia of the entire planet. The quantity $B - A$ is a measure of the degree to which the planet is prolate, as expressed by the second degree, second order gravitational coefficient C_{22} (Anderson *et al.* 1987) given by

$$C_{22} = \frac{(B-A)}{4MR^2} = (1 \pm 0.5) \times 10^{-5}. \tag{1.2}$$

The quantities M and R denote the planetary mass and radius, respectively. The polar moment of inertia C is a measure of resistance to changes in rotation rate and acts to reduce the amplitude of libration in equation (1.1). The axes A, B and C in (1.1) are the moments of inertia for the entire planet, which implies that the whole planet participates in the libration. However, if the entire core or at least its outermost region is fluid, the silicate shell (mantle and crust) will effectively be decoupled from the core and the libration would no longer be that of the whole planet. In this case, only the outer rigid shell would participate in the libration and the relevant moments of inertia should be that of the silicate shell alone.

Measurement of the amplitude of libration therefore provides a mechanism for remotely determining the existence of a fluid core (Peale, 1976; 2002). Margot *et al.* (2007) employed this technique to compare Mercury's observed libration amplitude to the expected amplitude for a rigid planet. They found that the observed amplitude, as measured by radar speckle data was twice as large ($\phi_0 = 35.8 \pm 2$ arcsec) compared to that expected from a solid planet. This conclusive evidence suggests that Mercury's mantle is decoupled from a

core that is at least partially molten, with only the mantle[2] participating in the libration. However, a possible weakness in the work of Peale (1976; 2002) and Margot *et al.* (2007) is the assumption that the entire core is perfectly spherical and therefore does not contribute to the difference in equatorial moments of inertia for the whole planet (i.e. $B - A = B_m - A_m$, where subscript m refers to the mantle). In reality, the prolate shape of the mantle will force the whole core to occupy a similar prolate shape, such that the difference in equatorial moments of inertia of the core cannot be neglected (see section 3.1). In Margot *et al*'s models for which only the silicate shell participates in the libration, the assumption that the libration amplitude $\phi_0 \propto \frac{B-A}{C_m}$ is made, when a more accurate representation is $\phi_0 \propto \frac{B_m - A_m}{C_m}$. This alteration makes the problem more difficult to solve; instead of making the assumption that $B - A = B_m - A_m$ and using measurements of C_{22} to find its numerical value, it is necessary to determine $B_m - A_m$ in isolation for the mantle, in such a way that both ϕ_0 and C_{22} are matched for a given model of Mercury's internal structure (see section 3.2).

1.2.2 Core-Mantle Coupling

Previous studies on Mercury's libration (e.g. Peale *et al.* 2002) investigated the effects of several coupling mechanisms (magnetic, viscous, gravitational and topographic) between the mantle and core, but concluded that each is likely too small to significantly influence the libration. However, a similar study by Van Hoolst *et al.* (2007) on the Galilean satellite Europa has revealed that gravitational coupling plays a significant role in Europa's libration. In this paper, we revisit only gravitational coupling between the mantle and inner

[2]From hereon the term 'mantle' will refer collectively to the mantle plus crust.

core, and provide a quantitative investigation into the interior conditions required for inner core-mantle coupling to affect the libration. Magnetic torques between the mantle and fluid core (Rochester, 1960) caused by flux shear are omitted in our discussion, since estimates of the magnitude of magnetic coupling on Mercury are at least three orders of magnitude smaller than typical estimates for gravitational coupling (Peale *et al.* 2002). Alternative studies by analogy with Earth (e.g. Love & Bloxham, 1994), further suggest that magnetic coupling is several orders of magnitude smaller than gravitational coupling. We also omit topographic coupling at the CMB between the fluid core and mantle due to its almost negligible influence on the libration amplitude (Rambaux *et al.* 2007). Viscous coupling between the mantle and fluid core is similarly rejected, since it has been shown by Peale *et al.* (2002) that a fluid core kinematic viscosity of $\nu \sim 10^4$ m^{2}s^{-1} is necessary for the core to be coupled with the mantle at the 88 day period. Because this value is many times larger than typical planetary estimates of $\nu \sim 10^{-5}$ m^{2}s^{-1} (e.g. Gans, 1972), it is highly unlikely that viscous coupling will affect the forced libration signature.

We first consider a three layer model of Mercury consisting of a solid mantle, a fluid outer core and solid inner core. The equatorial ellipticity of Mercury's mantle induces a perturbation in the surfaces of constant gravitational potential throughout the whole of the core. This perturbation forces the equipotential surfaces in the core to occupy an ellipsoidal form similar to that of the mantle. As a result, both the solid inner and fluid outer cores deform to the prolate shape imposed by the mantle (figure 1.2a). The mantle and inner core, in isolation, are expected to have different libration amplitudes (see section 4.1). This causes the axis of the mantle's minimum moment of inertia ψ_m to misalign with that of the inner core ψ_s, and a gravitational torque is

established between the two (figure 1.2b). The quantities ψ_m and ψ_s represent the angular displacement of the mantle and inner core respectively from the unperturbed state shown in figure 1.2a. The torque acts to realign the axes, and a rigid rotation of inner core ensues. An equal and opposite torque is also imposed on the mantle from the inner core, which acts to decrease the amplitude of the mantle libration.

The inability of the fluid outer core to withstand shear stress results in its continuous deformation over the timescale of the 88 day libration period, in order to accommodate the change in gravitational potential. Thus, the fluid core does not undergo a rigid body rotation. In contrast to the fluid core, we make the assumption that on short timescales ($\sim$ 88 days), the inner core acts as a rigid body, and its rotation cannot be compensated by viscous deformation. The misalignment that ensues between the mantle and inner core provides a means to initiate a *free-mode* of oscillation, which is a mechanism for the transfer of angular momentum between the mantle and inner core. On theoretical grounds, the gravitational free-mode should be visible in observations of Mercury's spin rate, with the spin rate being a superposition of the mean rotation, 88 day libration, the gravitational free-mode and the free libration of the mantle (discussed in section 4.1).

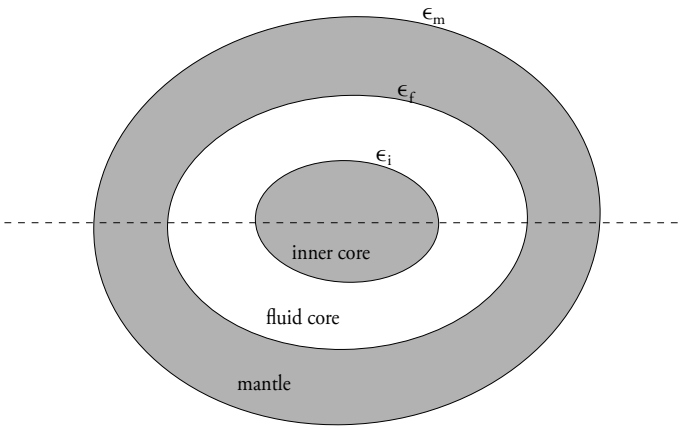

(a)

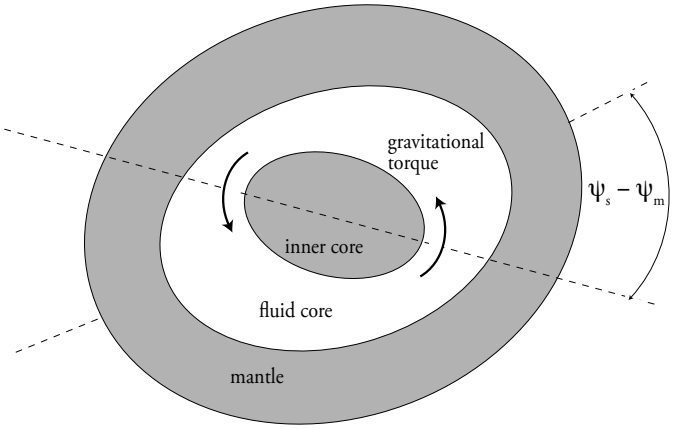

(b)

Figure 1.2: (a) Top down view of unperturbed state. Axes of minimum moment of inertia (dashed line) for the mantle and inner core are aligned. Mantle, CMB and core ellipticity denoted by ϵ_m, ϵ_f and ϵ_i respectively (see chapter 3). (b) Differential rotation between mantle and inner core causes angular separation $(\psi_s - \psi_m)$ between the two. The resulting gravitational torque acts to realign the axes, establishing an oscillatory free-mode. Figure (b) does not necessarily reflect the exact orientation of ψ_m and ψ_s.

1.3 The Role of the Inner Core on Mercury's Libration

The period of the free gravitational mode is controlled by the magnitude of the torque imposed by the mantle, and also the polar moments of inertia of both the mantle and inner core. Since these quantities are dependent on the planet's interior geometry, the period of the free-mode presents an indirect method of probing Mercury's interior.

The intent of this project is to investigate the effects of gravitational coupling between the mantle and inner core on Mercury's 88 day libration. We also look at the conditions that are necessary for the free-mode to play a role in the planet's rotation. By following the growth of the inner core from an initial, entirely fluid core to a final, fully solidified core, we calculate the magnitude of the gravitational couple and moments of inertia for a range of core geometries and initial core sulphur concentrations. We also assess the effect of the free-mode on Mercury's spin rate by numerically solving the governing set of coupled differential equations, and comparing the modeled solutions with current observations. Finally, we measure the quality of the fit between each of the modeled solutions and current observations with the aim of finding a preferential interior planetary structure.

Chapter 2 outlines the details concerning the model and describes how the core composition evolves over time. Chapter 3 features a complete discussion on mantle-inner core coupling, focusing primarily on developing expressions for the gravitational torque and the shape of equipotential surfaces throughout the planet. In chapter 4, the equations of motion that govern Mercury's rotation are introduced, along with a quantitative technique for comparing simulated and observed spin rates. Finally, results and discussions are pro-

vided in chapter 5, where we show how comparisons between modeled and observed spin rates provide an insight into Mercury's interior geometry.

Chapter 2

Modelling Mercury's Interior

Our simple model of Mercury's interior consists of three layers: a mantle, a fluid outer core and a solid inner core. We choose to incorporate the crust as part of the mantle due to its relatively small thickness. Because Mercury is small, compression effects are not likely to be significant, and densities do not vary much with radial distance from the planet's centre. For this reason, each of the layers is chosen to be homogeneous in its structure and composition, with density contrasts only at the surface, the CMB and the inner-core boundary (ICB). We choose a typical silicate density of $\rho_m = 3300$ kg m^{-3} for the mantle (Rivoldini *et al.* 2009); this value is used throughout the study. The density of the fluid core (ρ_f) and solid inner core (ρ_s) must be chosen such that Mercury's bulk mass and density, as shown in table 1.1, are matched. To do this, we follow a similar approach to van Hoolst & Jacobs (2003) by considering the compositional properties of the interior as the planet undergoes cooling. As a result, the model is not only constrained by bulk parameters such as mean density, but also by conditions that determine the chemical composition of the core as the planet evolves. As we will see, the volume and densities of

each of the mantle, fluid core and inner core can be completely determined by specifying only two parameters; the inner core radius and initial core sulphur concentration (see section 2.1). For all combinations of inner core radii and sulphur concentrations, the model remains consistent with the bulk parameters shown in table 1.1.

2.1 Initial Composition of an Entirely Liquid Core

We begin with an initial two-layer model in which Mercury's core is entirely liquid, and follow the growth of the solid inner core until the entire core has become solid. The growth of the inner core is due to the cooling of the planet, but we do not consider temperature evolution with time. Alternatively, we consider the change in density and composition of the core at the onset of cooling. We assume the core to be composed mostly of iron (Fe), with traces of the light element sulphur in the form of iron sulphide (FeS). Other light elements are undoubtedly present, but are not included here since their inclusion will not likely affect the results (van Hoolst & Jacobs, 2003). The significance of including sulphur as a light element is demonstrated in its ability to lower the freezing temperature of the Fe-FeS metallic mixture. However, the concentration of sulphur in Mercury's core is currently unknown. Critically, it depends on the location of Mercury's accretion in the early Solar System (Wetherill, 1988). If Mercury accreted at its current location, it is expected that light element concentration would be significantly diminished as volatile fractions were among the first ejected from the cooling Solar nebula (Lewis, 1988). However, if Mercury formed in the same feeder zones as Venus,

Earth and Mars, we might expect the concentration to be higher and closer to that of those planets. In the model used here, we range sulphur concentration in the initial, entirely fluid core χ_S^{in} from 0.1 to 14 weight percentage. The lower value represents a core that is almost entirely Fe, while the upper limit is chosen to match the predicted sulphur concentration of Mars' core (Longhi *et al.* 1992). The initial state of the core is thus uniquely defined by core sulphur concentration, and we follow inner core growth from this initial state. One distinct advantage of using composition of the core as a chemical constraint is that every possible interior structure that Mercury might exhibit can be prescribed by knowledge of only the initial core sulphur concentration and inner core radius (as will be seen in later chapters).

Both Fe and FeS can occupy a number of phases, depending on pressure and temperature. At typical conditions of Mercury's core, iron is in the γ phase (Anderson, 2003) and FeS is in phase III (high pressure phase). It should be noted that although phases IV and V exist at these pressures and temperatures (Fei *et al.* 1995), models with these included vary little in comparison from those with FeS III (Harder & Schubert, 2001). Density values for γ iron and phase III FeS at core conditions are taken from van Hoolst & Jacobs (2003) and shown in table 2.1 below. Under mean core conditions, the average pressure and temperature are taken to be 20 GPa and 1700 K respectively (Baumgardner & Anderson, 1981; Stevenson *et al.* 1983). Also given in table 2.1 are the Fe and FeS densities in liquid form, which are 3.5% lower than their solid counterparts.

Table 2.1: Densities of solid and liquid Fe and FeS under core conditions

Parameter	Symbol and value
Density of solid Fe (kg m^{-3})	$\rho_{Fe}^{solid} = 8160$ kg m^{-3}
Density of solid FeS (kg m^{-3})	$\rho_{FeS}^{solid} = 5808$ kg m^{-3}
Density of liquid Fe (kg m^{-3})	$\rho_{Fe}^{liquid} = 7874$ kg m^{-3}
Density of liquid FeS (kg m^{-3})	$\rho_{FeS}^{liquid} = 5605$ kg m^{-3}

For an initial core composed of pure iron, the core density would be exactly ρ_{Fe}^{liquid}, since the initial core is fluid. In contrast, a core composed of pure iron sulphide would have a density ρ_{FeS}^{liquid}. In reality the core composition is likely to be in between these two extremes i.e. with a sulphur concentration chosen here to be between 0.1 and 14 wt%. The density of the initially liquid core is then a function of sulphur content, given by (e.g. van Hoolst & Jacobs, 2003)

$$\rho_f^{in} = \left(\frac{\chi_{FeS}^{in}}{\rho_{FeS}^{liquid}} + \frac{1 - \chi_{FeS}^{in}}{\rho_{Fe}^{liquid}} \right)^{-1}, \tag{2.1}$$

where χ_{FeS}^{in} is the initial concentration of FeS in the core. The term χ_{FeS}^{in} is not the same as χ_S^{in}. Although we define the core composition in terms of sulphur concentration χ_S^{in}, sulphur does not reside in elemental form in the core, but in the compound form, FeS. The concentration of FeS is related to the concentration of sulphur[1] through,

$$\chi_{FeS}^{in} = \frac{\chi_S^{in}}{0.3648} \tag{2.2}$$

where 0.3648 is the ratio of atomic mass between sulphur and FeS. In order to match the overall mass of the planet, equation (2.1) requires changes in χ_S^{in} to be accompanied with a change in core radius, r_f. The core radius can be

[1]In the above and all subsequent equations, chemical compositions χ, take on their decimal, rather than percentage form.

calculated by expressing the total mass of the planet as

$$M = M_{core} + M_{mantle}$$

$$\bar{\rho} r_e^3 = \rho_f^{in} r_f^3 + \rho_m (r_e^3 - r_f^3)$$

and rearranging to give

$$r_f = r_e \left(\frac{\bar{\rho} - \rho_m}{\rho_f^{in} - \rho_m} \right)^{1/3}, \tag{2.3}$$

where $r_e = 2440$ km is the planetary radius and $\bar{\rho} = 5427$ kg m^{-3} is the mean planetary density. The subscripts e, m, f and s denote whole planet, mantle, fluid core and solid core respectively unless otherwise stated. Table 2.2 shows the corresponding core densities and radii for a range of initial sulphur concentrations χ_S^{in}. These values serve as a set of initial outer core radii from which we subsequently allow the growth of an inner core.

Table 2.2: Core density and radius as a function of initial sulphur concentration

χ_S^{in} (wt%)	ρ_f^{in} (kg m^{-3})	r_f (km)
0.1	7866	1891
2	7703	1915
4	7540	1939
6	7383	1963
8	7232	1988
10	7088	2013
12	6949	2038
14	6815	2064

2.2 Interior Evolution and Core Precipitation

As Mercury cools, the initially fluid core begins to freeze and the thickness of the fluid core shell decreases. The freezing begins at the centre of the planet and a solid inner core begins to grow in an outward radial fashion. This is a result of the melting temperature of iron increasing more rapidly towards the centre, due to the higher pressure, than the real temperature of the material (Stevenson *et al.* 1980). Recent experimental studies (e.g. Chen *et al.* 2008) have also suggested that precipitation of an inner core may arise from solidification of iron near the CMB as a result of cooling. The consequent 'snow' that forms as the iron falls back towards the planet centre may also be a valid mechanism for inner core growth. In either case, we neglect the light element concentration in the solid core and assume that only pure iron precipitates out of the fluid core to form the solid core. Upon solidification, the lighter elements, most notably sulphur, will remain the outer core. Not only does this increase the concentration of lighter elements in the outer core as the solid core continues to grow, but will also induce convective motions as a result of compositional buoyancy (Braginsky, 1964). Such convective motions may be relevant for a dynamo generated, global magnetic field.

Invoking homogeneity of the inner and outer cores, we find that upon precipitation of an inner core, the density of the inner and outer cores become

$$\rho_s = \rho_{Fe}^{solid} \tag{2.4}$$

and

$$\rho_f = \left(\frac{\chi_{FeS}}{\rho_{FeS}^{liquid}} + \frac{1 - \chi_{FeS}}{\rho_{Fe}^{liquid}} \right)^{-1} \tag{2.5}$$

respectively. Equation (2.5) is of the exact same form as (2.1), but now χ_{FeS}

changes with inner core growth as sulphur is excluded and remains in the outer core. To determine how χ_{FeS} depends on r_s, we assume that no mass exchange occurs between the whole core and the mantle, so that the mass of the whole core remains constant over time. Applying mass conservation of the core we find

$$\frac{M_f}{M_{core}} = \frac{\chi^{in}_{FeS}}{\chi_{FeS}}. \tag{2.6}$$

Substituting $M_f = M_{core} - M_s$ reveals

$$\chi_{FeS} = \frac{\chi^{in}_{FeS}}{1 - \frac{M_s}{M_{core}}}, \tag{2.7}$$

which results in the FeS enrichment of the outer core as the mass of the inner core increases. Using equations (2.5) and (2.7) ensures that mass is conserved in all possible interior configurations. Figure 2.1 demonstrates the change in χ_{FeS} with inner core radius for a range of initial sulphur concentrations. The flattening of curves at $\chi_{FeS} = 0.61$ represents the *eutectic limit*, a feature of the model that is discussed in the following section.

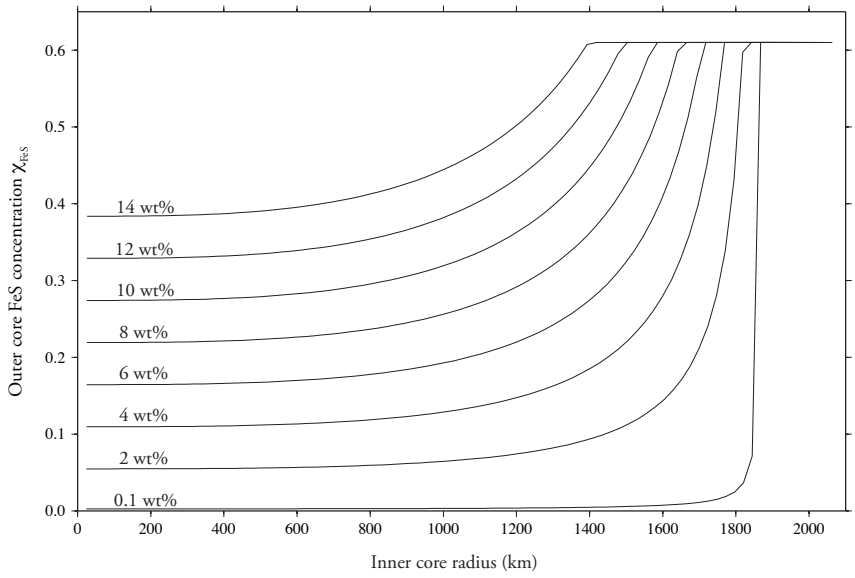

Figure 2.1: Outer core FeS concentration χ_{FeS} versus inner core radius. Lines represent different initial core sulphur concentrations χ_S^{in}.

2.3 The Eutectic Limit

As the solid iron core grows in size, the sulphur content in the diminishing liquid core increases. Evidently, the solid core cannot grow until the whole core is solidified since this would require the solid core to consume the sulphur that had previously resided in the liquid part. If this was the case, the inner core would no longer consist of pure iron and we would require the solidification of a mixture that is highly concentrated in FeS. However, there is a point known as the *eutectic limit* at which sulphur compounds are able to solidify. At this limit, the sulphur compound takes on a eutectic composition, which represents the single mixture of Fe and FeS that has a freezing temperature lower than any other Fe/FeS mixture. On a phase diagram, the eutectic point is characterised by a sharp minimum in the liquidus curve. Before the eutectic

point has been reached, we assume that no sulphur can solidify in the core (van Hoolst & Jacobs, 2003). From the eutectic point on, the fluid outer core continues to freeze and the solid deposits on the inner core have the same light element concentration as the fluid core, χ_{FeS}^{eut} (fig 2.2). From equation (2.7), it follows that the eutectic composition is reached when the inner core has a mass

$$M_s^{eut} = M_{core}\left(1 - \frac{\chi_{FeS}^{in}}{\chi_{FeS}^{eut}}\right). \tag{2.8}$$

This can be translated into an inner core radius by expressing the inner core radius in terms of the mass ratio M_s^{eut}/M_{core},

$$r_s^{eut} = \left[\frac{3}{4\pi}\frac{M_{core}}{\rho_s}\left(\frac{M_s^{eut}}{M_{core}}\right)\right]^{1/3}. \tag{2.9}$$

Substituting the result from (2.8), and recalling that inner core density is equal to ρ_{Fe}^{solid} reveals

$$r_s^{eut} = \left[\frac{3}{4\pi}\frac{M_{core}}{\rho_{Fe}^{solid}}\left(1 - \frac{\chi_{FeS}^{in}}{\chi_{FeS}^{eut}}\right)\right]^{1/3}. \tag{2.10}$$

The eutectic composition of Mercury's core, χ_{FeS}^{eut} has been experimentally determined to be 0.61 (Usselman, 1965). This value correlates to a 22% weight fraction of sulphur. After the liquid outer core has attained this composition, it will no longer change in composition, and will freeze on to the solid inner core. At this point, the inner core consists of two distinct layers: The inner layer with density $\rho_s = \rho_{Fe}^{solid}$ and radius r_s^{eut}, and an outer most layer of thickness $r_s - r_s^{eut}$ and density ρ_s^{eut} where

$$\rho_s^{eut} = \left(\frac{\chi_{FeS}^{eut}}{\rho_{FeS}^{liquid}} + \frac{1 - \chi_{FeS}^{eut}}{\rho_{Fe}^{liquid}}\right)^{-1}. \tag{2.11}$$

The effect of the inner core consisting of two layers has a small influence on the moments of inertia of the inner core and the gravitational torque between

the inner core and mantle, as we discuss in chapter 3.2.

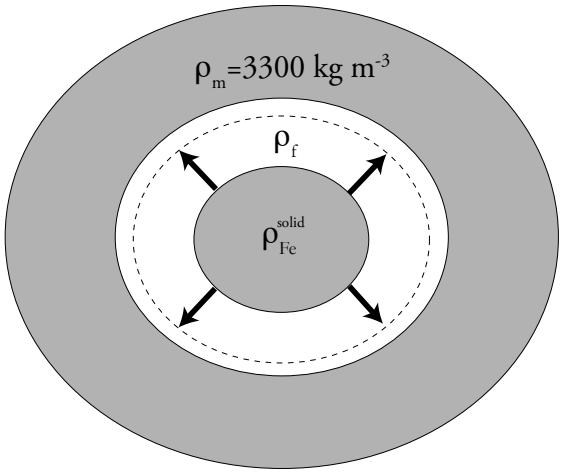

Figure 2.2: Inner core growth. Dashed line represents the eutectic radius r_s^{eut}, beyond which the solid deposit takes on the eutectic composition.

As soon as the eutectic point has been reached, compositional buoyancy ceases due to the lack of exchange of sinking iron and buoyant light elements between the fluid and solid cores. This remains an important power source for convection, and it is uncertain whether a dynamo generating a global magnetic field can exist beyond the eutectic limit (Braginsky, 1964). If early measurements from Messenger and BepiColombo detect temporal changes in the global magnetic field, indicating an active, self-sustaining dynamo, it will point to an inner core radius that is likely smaller than r_s^{eut}.

2.4 Core Contraction

It was assumed in section 2.2 that no mass exchange occurred between the mantle and core. This assumption enabled a constant mass core to be maintained as the inner core increased in radius. Following mass conservation

of the mantle, one would expect the core radius r_f to also remain constant as the inner core grows, implying that the mean density of the whole core must remain equal to ρ_f^{in}. However, table 2.1 shows that the difference in density between solid Fe (FeS) and their liquidus counterparts is 3.5%. The combination of a 3.5% density increase of iron upon solidification and applying mass conservation of the core inevitably creates a scenario in which it is necessary for the core (and also the whole planet) to contract during the planet's evolution. As an example we consider an initial scenario in which the whole core is completely fluid, and a final scenario in which the core has completely solidified. The solid core has density that is 3.5% greater than the liquid case. In order to maintain mass conservation of the core, a decrease in core (and planetary) radii is required. The change in core radius is given by

$$\frac{\Delta r_f}{r_f} = -\frac{1}{3}\frac{\Delta \rho_{core}}{\rho_{core}}, \tag{2.12}$$

where $\Delta\rho_{core}$ is the difference between initial core density and core density after solidification. Using values of core radii from table 2.2 it can be shown that the maximum decrease in r_f occurs for the highest sulphur concentration χ_S^{in} = 0.14, while the smallest radial contraction occurs for models with no sulphur content. For a concentration of $\chi_S^{in} = 0.14$, the decrease in r_f is approximately 24 km. In order to translate the decrease in core radius to the decrease in planetary radius, we use conservation of mantle volume to find

$$\frac{\Delta r_e}{r_f^2} = \frac{\Delta r_f}{r_e^2}. \tag{2.13}$$

Substituting values for $\chi_S^{in} = 0.14$ gives a maximum decrease in planetary radius of 16 km. Figure 2.3 shows the change in both core and planetary radii as a function of inner growth for a sulphur concentration of $\chi_S^{in} = 0.14$.

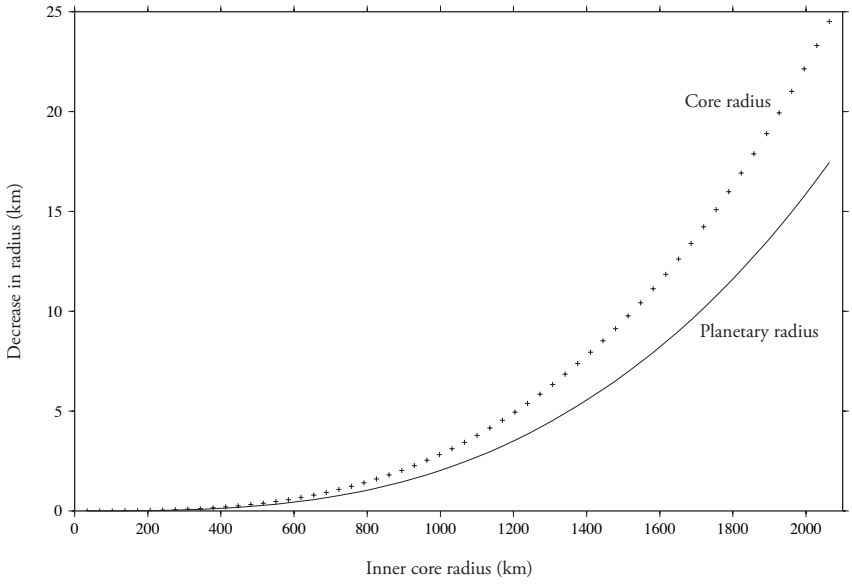

Figure 2.3: Decrease in radius of the core and planet as a function of inner core radius for $\chi_S^{in} = 0.14$.

A comparison between the radial contraction for models with core sulphur concentrations of $\chi_S^{in} = 0.14$ versus $\chi_S^{in} = 0.001$ shows very little difference between the two. Figure 2.4 reveals a planetary radius decrease of 13 km after full solidification of the core. The small difference in values suggests that contraction of the planet due to inner growth gives little indication to Mercury's core sulphur content.

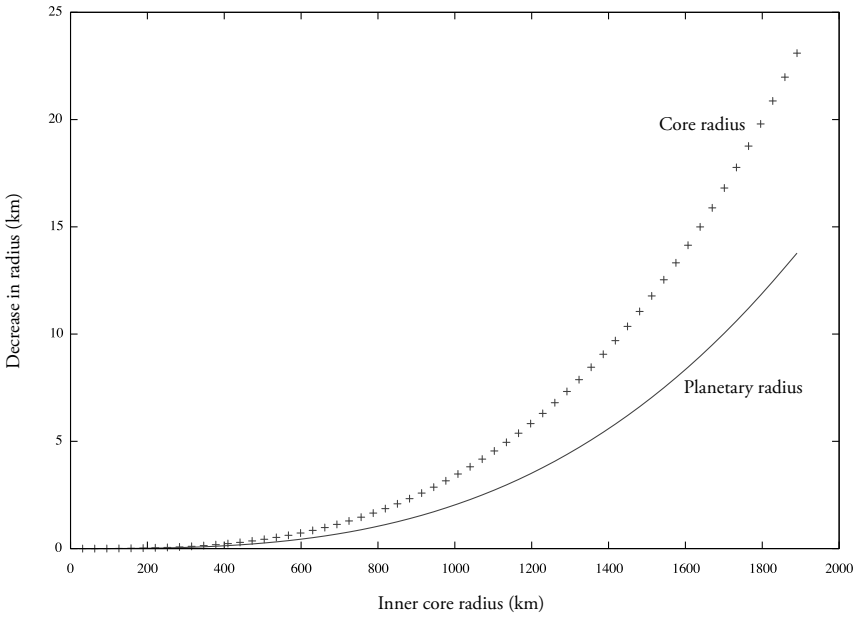

Figure 2.4: Decrease in radius of the core and planet as a function of inner core radius for $\chi_S^{in} = 0.001$.

Although the effects of core contraction have been included in the models of van Hoolst & Jacobs (2003) and Schubert *et al.* (1988), we choose not to include them here. The magnitude of the planet's contraction is approximately 0.5% of the planetary radius, and for this reason, it is unlikely that planetary contraction will have a measurable effect on our results. Including the effects of core contraction would only add unnecessary complexity to the model, and our goal is to assess the effects of gravitational coupling between the mantle and inner core to a first order approximation.

Chapter 3

Gravitational Interaction Between the Mantle and Inner Core

Up to this point we have been able to use the free variables χ_S^{in} and r_s to completely determine a density model for all possible Mercury interior configurations. We are now in a position to begin developing the framework in which we can estimate the magnitude of the gravitational couple between the mantle and inner core. We begin with a discussion on how the shape of equipotential surfaces in the core deform in response to the prolate shaped mantle. In sections 3.1 and 3.2 we write expressions for the physical shape of the mantle, CMB and core in terms of model parameters, in a way that maintains consistency with observations of C_{22}. We introduce the concept of a gravitational torque between the mantle and inner core in section 3.3, and derive appropriate equations to estimate its magnitude. Finally, in section 3.4, we use the concept of mantle-inner core angular momentum exchange and how it can be

used to approximate the gravitational free-mode period.

3.1 Deformation of Material Surfaces in the Core

In order to calculate the magnitude of the couple between the mantle and inner core, it is necessary to determine the shape of gravitational equipotential surfaces inside the core. We assume a mantle of density $\rho_m = 3300$ kg m^{-3}, with a simple, equatorial elliptical shape defined by ϵ_m and ϵ_f at the surface and the CMB respectively. The subscript notation used for ϵ varies slightly from what has been used previously; m still refers to mantle, but f now represents the solid (mantle) side of the CMB.

The manner in which hydrostatic deformation occurs in response to a gravitational forcing from the mantle has been derived in the studies of Wahr & de Vries (1989) and Dehant & Wahr (1991). Were Mercury not rotating and everywhere in hydrostatic equilibrium, variations in pressure (p_0), density (ρ_0) and gravitational acceleration (g_0) would be purely radial and related by

$$\frac{\partial}{\partial r} p_0(r) = -\rho_0(r) g_0(r), \tag{3.1}$$

where $g_0(r)$ is related to the gravitational potential Φ_0 by

$$g_0(r) = \frac{\partial}{\partial r} \Phi_0(r). \tag{3.2}$$

At long wavelength (low spherical harmonic degree), departures with respect to this spherically symmetric, hydrostatic reference state are dominantly the result of lateral heterogeneities in the mantle and crust which deform the planet

to give it a prolate figure. In order to retain a purely homogeneous ρ_m, we model these heterogeneities in terms of equivalent mass variations produced by ϵ_m and ϵ_f. The factors $\epsilon_{m,f}$ represent perturbations from this reference state and are a measure of the equatorial ellipticity of their respective components. The origin of Mercury's prolate figure is probably not due to Solar tidal forces, but a combination of a large impact, reorientation and despinning (Matsuyama & Nimmo, 2009). Mantle convection, whether it be currently maintaining Mercury's shape or a frozen in remnant from a time when active convection was occurring may also contribute to the planet's shape. The topography associated with Mercury's prolate shape leads to global variations in the gravitational potential. We express the gravitational potential Φ everywhere inside Mercury by a sum of its radial component $\Phi_0(r)$ and its deviation from spherical symmetry in terms of spherical harmonic functions Y_l^m with coefficients $\delta\Phi_l^m(r)$,

$$\Phi = \Phi_0(r) + \sum_l \sum_m \delta\Phi_l^m(r) Y_l^m. \tag{3.3}$$

To simplify the notation, from this point onward we drop the indices l and m on the spherical harmonic coefficients. Thus, $\delta\Phi \equiv \delta\Phi_l^m$, though it has to be understood that $\delta\Phi$ is the coefficient for one particular degree l and order m. This convention applies to the deviation of any quantity X; the notation δX represents one spherical harmonic coefficient of X.

Inside the core, the gravitational potential is related to density anomalies $\delta\rho$ through Poisson's equation,

$$\nabla^2 \delta\Phi = 4\pi G \delta\rho, \tag{3.4}$$

or in its expanded form (e.g. Dahlen, 1974),

$$\frac{\partial^2 \delta\Phi}{\partial r^2} + \frac{2}{r}\frac{\partial \delta\Phi}{\partial r} - \left[\frac{l(l+1)}{r^2} + \frac{4\pi G}{g_0}\frac{\partial \rho_0}{\partial r}\right]\delta\Phi = 0. \tag{3.5}$$

An exact solution can be found if $\frac{\partial \rho_0}{\partial r} = 0$. We have chosen constant density layers in our model in part for this convenience, revealing an exact solution given by

$$\delta\Phi = F g_0(r) r_f \left(\frac{r}{r_f}\right)^{l-1}, \tag{3.6}$$

where the coefficient F is

$$F = \frac{2l+1}{r_f}\left(\frac{\delta\Phi_M}{2(l-1)g_f + 4\pi G \rho_f r_f}\right). \tag{3.7}$$

The term $\delta\Phi_M$ represents the gravitational potential from density anomalies in the mantle and topography at the surface and CMB (measured at the CMB), and can be expressed in the generalised form

$$\delta\Phi_M(r_f) = \frac{4\pi G}{2l+1}\sum_j [\rho_0(d_j)]^+_- \frac{r_f^l}{d_j^{l-1}} \Delta h(d_j), \tag{3.8}$$

where $\Delta h(d_j)$ is the spherical harmonic coefficient of the displacement from the j-th density discontinuity with radius d_j. The notation $[X(d_j)]^+_-$ is used to represent the discontinuity in a quantity X at $r = d_j$. With our choice of a homogeneous mantle, density anomalies are not present and the only contribution to $\delta\Phi_M$ is from the prolateness of Mercury's mantle and CMB. Since the equatorial ellipticity of Mercury's surface and CMB are characterised by the $l = 2$, $m = 2$ component of $\delta\Phi_M$, we can note that $\Delta h(d_j) = \epsilon d_j$ where

ϵ is equatorial ellipticity, and expand equation (3.8) to give,

$$\begin{aligned}\delta\Phi_M &= \frac{4\pi G}{5}\big(- \rho_m r_f^2 \epsilon_m + (\rho_m - \rho_f) r_f^2 \epsilon_f\big) \\ &= -\frac{4\pi G}{5} r_f^2 \big(- \rho_m \epsilon_m + (\rho_m - \rho_f)\epsilon_f\big). \end{aligned} \tag{3.9}$$

The contribution of the elliptical surface and CMB to the imposed mantle gravitational potential $\delta\Phi_M$ induces the deformation of equipotential surfaces throughout the whole core, causing the whole core to occupy a similar elliptical profile to that of the mantle. It is possible to relate $\delta\Phi_M$ to the elliptical shape ($l = 2$, $m = 2$ component) of the core ϵ_i through

$$\epsilon_i = -F = -\frac{5}{r_f}\left(\frac{\delta\Phi_M}{2g_f + 4\pi G\rho_f r_f}\right). \tag{3.10}$$

A full explanation and derivation of (3.10) is covered in appendix C. The subscript i refers to the whole (fluid + solid) core due to the assumption that the inner core is also in hydrostatic equilibrium (see also appendix C). Because the whole core is thought to be in hydrostatic equilibrium (i.e. over long timescales gravity is sufficient to overcome rigidity), the physical shape of the core coincides with surfaces of constant gravitational potential and other material surfaces such as density. Therefore ϵ_i represents both the physical shape of the core, and also the shape of gravitational equipotential surfaces within the whole core. This is not the case for the mantle, which is known not to be in hydrostatic equilibrium from observations of C_{20} and C_{22}. Equation (3.10) may be re-written by substituting the result from (3.9) and replacing g_f with

$$g_f = \frac{GM_{core}}{r_f^2} = \frac{4\pi}{3} G\bar{\rho}_{core} r_f, \tag{3.11}$$

where $\bar{\rho}_{core}$ $(=\rho_f^{in})$ is the mean core density. The expression for ϵ_i can be

written as

$$\epsilon_i = k_m \epsilon_m + k_f \epsilon_f, \tag{3.12}$$

where

$$k_m = \frac{\rho_m}{\frac{2}{3}\bar{\rho}_{core} + \rho_f} \quad \text{and} \quad k_f = \frac{\rho_f - \rho_m}{\frac{2}{3}\bar{\rho}_{core} + \rho_f}. \tag{3.13}$$

It is evident from (3.12) that the elliptical shape of the whole core is determined by the ellipticity of both the mantle and the CMB. The amount to which either ϵ_m or ϵ_f contributes to ϵ_i is governed by the dimensionless factors k_m and k_f respectively. Both factors can be determined easily, since they depend only on density structure. This is an expected property since it is the density structure that governs the shape of gravitational potential surfaces inside the core, and therefore the ellipticity of the entire core.

3.2 Deformation of Material Surfaces in the Mantle and at the Core-Mantle Boundary

In the previous section we showed that the ellipticity of the whole core ϵ_i can be written in terms of the ellipticity of the mantle ϵ_m and CMB ϵ_f. It is necessary to express ϵ_m and ϵ_f in terms of known quantities, which in turn can be determined from the free variables χ_S^{in} and r_s. A requirement of the expressions for $\epsilon_{m,f}$ is that they must be consistent not only with $C_{22} = 1 \times 10^{-5}$, but also (albeit limited) observations of libration amplitude ϕ_0 for all model interiors. Since the eccentricity e of Mercury's orbit is assumed constant, the constraint on ϕ_0 is effectively a condition on the moment of inertia ratio $\frac{B_m - A_m}{C_m}$ (see equation (1.1)). The moment of inertia ratio is referred to, in shorthand,

as $\Delta\gamma_m$, and any changes in $\epsilon_{m,f}$ must be accompanied by an adjustment in $\Delta\gamma_m$. Using current observations of libration amplitude $\phi_0 = 35.8 \pm 2$ arcsec and orbital eccentricity $e = 0.206$, equation (1.1) can be rearranged to yield $\Delta\gamma_m = 2.03 \times 10^{-4}$. We use this value as a constraint in our formulations of ϵ_m and ϵ_f.

We begin determining ϵ_m and ϵ_f by considering the two constraining equations,

$$\Delta\gamma_m = \frac{B_m - A_m}{C_m} \quad \text{and} \tag{3.14a}$$

$$C_{22} = \frac{B - A}{4Mr_e^2}. \tag{3.14b}$$

Using the respective definitions of $B - A$, $B_m - A_m$ and C_m

$$B - A = \frac{8\pi}{15}\int_0^{r_e} \rho_0(r)\frac{\partial}{\partial r}\big(r^5\epsilon(r)\big)dr, \tag{3.15}$$

$$B_m - A_m = \frac{8\pi}{15}\int_{r_f}^{r_e} \rho_0(r)\frac{\partial}{\partial r}\big(r^5\epsilon(r)\big)dr, \tag{3.16}$$

$$C_m = \frac{8\pi}{3}\int_{r_f}^{r_e} \rho_0(r)r^4 dr, \tag{3.17}$$

and expanding using our constant density approximation, we find

$$B - A = \frac{8\pi}{15}\Big[\rho_m(r_e^5\epsilon_m - r_f^5\epsilon_f) + \rho_f(r_f^5\epsilon_f - r_s^5\epsilon_i) + \rho_s(r_s^5\epsilon_i)\Big], \tag{3.18}$$

$$B_m - A_m = \frac{8\pi}{15}\Big[\rho_m(r_e^5\epsilon_m - r_f^5\epsilon_f)\Big], \tag{3.19}$$

$$C_m = \frac{8\pi}{15}\rho_m(r_e^5 - r_f^5). \tag{3.20}$$

Substituting the above results into (3.14a) and (3.14b) reveals

$$\Delta\gamma_m = \frac{\epsilon_m - \left(\frac{r_f}{r_e}\right)^5 \epsilon_f}{1 - \left(\frac{r_f}{r_e}\right)^5} \quad \text{and} \tag{3.21a}$$

$$C_{22} = \frac{2\pi}{15Mr_e^2}\left[\rho_m r_e^5 \epsilon_m + (\rho_f - \rho_m) r_f^5 \epsilon_f + (\rho_s - \rho_f) r_s^5 \epsilon_i\right]. \tag{3.21b}$$

We simplify (3.21b) by dividing through by r_e^5 and writing M in terms of the mean planetary density $\overline{\rho} = 5427\text{kg m}^{-3}$ and radius r_e. Using the result $\epsilon_i = k_m\epsilon_m + k_f\epsilon_f$ which was derived in section 3.1, enables a system of two equations with two unknowns. The resulting simultaneous equations are

$$\Delta\gamma_m\left[1 - \left(\frac{r_f}{r_e}\right)^5\right] = \epsilon_m - \left(\frac{r_f}{r_e}\right)^5 \epsilon_f \qquad \text{and} \tag{3.22a}$$

$$\begin{aligned} 10\bar{\rho}C_{22} = &\left[\rho_m + k_m(\rho_s - \rho_f)\left(\frac{r_s}{r_e}\right)^5\right]\epsilon_m \\ &+ \left[(\rho_f - \rho_m)\left(\frac{r_f}{r_e}\right)^5 + k_f(\rho_s - \rho_f)\left(\frac{r_s}{r_e}\right)^5\right]\epsilon_f. \end{aligned} \tag{3.22b}$$

Manipulating the simultaneous equations to eliminate ϵ_m reveals

$$\epsilon_f = \frac{10\bar{\rho}C_{22} - \Delta\gamma_m\left[1 - \left(\frac{r_f}{r_e}\right)^5\right]\left[\rho_m + k_m(\rho_s - \rho_f)\left(\frac{r_s}{r_e}\right)^5\right]}{\rho_f\left(\frac{r_f}{r_e}\right)^5 + (\rho_s - \rho_f)\left(\frac{r_s}{r_e}\right)^5\left[k_f + k_m\left(\frac{r_f}{r_e}\right)^5\right]}. \tag{3.23}$$

Using a similar technique to eliminate ϵ_f we arrive at the expression

$$\epsilon_m = \frac{10\bar{\rho}C_{22}\left(\frac{r_f}{r_e}\right)^5 - \Delta\gamma_m\left[1 - \left(\frac{r_f}{r_e}\right)^5\right]\left[(\rho_f - \rho_m)\left(\frac{r_f}{r_e}\right)^5 + k_f(\rho_s - \rho_f)\left(\frac{r_s}{r_e}\right)^5\right]}{\rho_f\left(\frac{r_f}{r_e}\right)^5 + (\rho_s - \rho_f)\left(\frac{r_s}{r_e}\right)^5\left[k_f + k_m\left(\frac{r_f}{r_e}\right)^5\right]}. \tag{3.24}$$

Equations (3.23) and (3.24) allow us to obtain specific values of ϵ_m and ϵ_f from any given interior structure in terms of r_s and χ_S^{in}. Significantly, they are both consistent with observations of $\Delta\gamma_m$ and C_{22} for all of our models

of Mercury's interior. The three equations (3.12), (3.23) and (3.24) take on a slightly different form beyond the eutectic radius because of the additional layer on top of the inner core that must be accounted for. Their modified expressions are given in appendix B.

With equations (3.12), (3.23) and (3.24), the ellipticity of the core, CMB and mantle have been written in terms of known parameters. It is important to reiterate that all of the parameters in these equations (and throughout this study) can be determined in terms of χ_S^{in} and r_s; they are the only free variables of the full system. Each combination of χ_S^{in} and r_s produces a model of Mercury's interior that not only satisfies its bulk mass and density, but also, through ϵ_m and ϵ_f, matches observed values of C_{22} and $\Delta\gamma_m$.

3.3 Deriving the Gravitational Torque

In the previous two sections we have taken a basic density model of Mercury's interior and assessed the hydrostatic deformation of the core as a result of an imposing gravitational potential from a prolate mantle. The ellipticities of the mantle and CMB have also been expressed in a way such that they are consistent with observations of C_{22} and the moment of inertia ratio $\frac{B_m - A_m}{C_m}$, while also being fully determined by the free variables χ_S^{in} and r_s.

It is now possible to consider the gravitational interaction between the mantle and inner core, and we proceed by deriving the gravitational torque between the two. The torque, Γ is dependent on both the interior structure of the planet and the angular displacement between the mantle and inner core:

$$\Gamma = \overline{\Gamma} \sin 2(\psi_s - \psi_m). \tag{3.25}$$

The coupling parameter, $\overline{\Gamma}$ depends purely on Mercury's interior geometry, and can be written as (Dumberry, 2008)

$$\overline{\Gamma} = \frac{4\pi G}{5} \left|\overline{\rho\epsilon} + \rho_f \epsilon_i\right| \left|(B_s - A_s) - (B_s' - A_s')\right| \tag{3.26}$$

where G is the gravitational constant. The term $(B_s - A_s)$ represents the difference in equatorial moments of the inner core, and is defined by

$$B_s - A_s = \frac{8\pi}{15} \int_0^{r_s} \rho(r) \frac{\partial}{\partial r}\big(r^5 \epsilon(r)\big) dr, \tag{3.27}$$

which, for our assumption of constant density can be simplified as

$$B_s - A_s = \frac{8\pi}{15} \rho_s r_s^5 \epsilon_i. \tag{3.28}$$

The term $(B_s' - A_s')$ is evaluated by replacing $\rho(r)$ with ρ_f in equation (3.27),

$$\begin{aligned} {B_s}' - {A_s}' &= \frac{8\pi}{15} \int_0^{r_s} \rho_f \frac{\partial}{\partial r}\big(r^5 \epsilon(r)\big) dr \\ &= \frac{8\pi}{15} \rho_f r_s^5 \epsilon_i. \end{aligned} \tag{3.29}$$

Physically, B_s' and A_s' represent the equatorial moments of inertia of a body having the shape of the inner core but with density ρ_f. Only the elliptical components ($l = 2$, $m = 2$) of the core, mantle and CMB are considered, since it is these components that are responsible for the difference in equatorial moments of inertia, $B - A$. In reality however, the gravitational torque depends on higher degrees ($l \geq 2$), but the contribution from these is expected to be much smaller than the dominant $l = 2$ component due to spatial attenuation. As a first order approximation, only the $l = 2$ component of the gravitational torque is considered. The term $\overline{\rho\epsilon}$ characterises the deviation of mass from

spherical symmetry and is given by

$$\begin{aligned}\overline{\rho\epsilon} &= \int_{r_s}^{r_e} \rho(r)\frac{\partial}{\partial r}\epsilon(r)dr \\ &= \int_{r_s}^{r_f} \rho(r)\frac{\partial}{\partial r}\epsilon(r)dr + \int_{r_f}^{r_e} \rho(r)\frac{\partial}{\partial r}\epsilon(r)dr,\end{aligned} \tag{3.30}$$

which, again, for constant density layers can be simplified to

$$\overline{\rho\epsilon} = \rho_f(\epsilon_f - \epsilon_i) + \rho_m(\epsilon_m - \epsilon_f). \tag{3.31}$$

Substituting the results of (3.28), (3.29) and (3.31) back into (3.26), we obtain a simplified expression for the coupling constant,

$$\overline{\Gamma} = \left(\frac{4\pi G}{5}\right)\left(\frac{8\pi}{15}\right) r_s^5 \epsilon_i \big(\rho_s - \rho_f\big)\big(\rho_f\epsilon_f + \rho_m\epsilon_m - \rho_m\epsilon_f\big). \tag{3.32}$$

Noting that the polar moment of inertia of the inner core C_s is defined by

$$\begin{aligned}C_s &= \frac{8\pi}{3}\int_0^{r_s} \rho(r) r^4 dr \\ &= \frac{8\pi}{15}\rho_s r_s^5,\end{aligned} \tag{3.33}$$

we can rearrange (3.32) as

$$\overline{\Gamma} = \left(\frac{4\pi G}{5}\right)\left(1 - \frac{\rho_f}{\rho_s}\right) C_s\epsilon_i\big((\rho_f - \rho_m)\epsilon_f + \rho_m\epsilon_m\big). \tag{3.34}$$

Equation (3.34) relates the magnitude of the coupling constant to parameters that can be calculated upon specification of χ_S^{in} and r_s. The addition of the thin layer with density ρ_s^{eut} on top of the inner core, which occurs after the eutectic composition has been attained, necessitates a small change in our expression for $\overline{\Gamma}$. This adjustment is shown in appendix B.

The estimation of the magnitude of the coupling constant enables us to look at the dynamics of Mercury's gravitational free-mode, which arises after the mantle and inner core are misaligned from their equilibrium positions.

3.4 Inner Core-Mantle free-mode

The free-mode of oscillation that occurs between the mantle and inner core allows for angular momentum exchange between the two. We can determine the effects of gravitational coupling and polar moments of inertia on the free-mode period by considering the angular momentum of both the mantle and inner core. The angular momentum balance in a planetary fixed reference frame is given by

$$\frac{d\mathbf{H}}{dt} + \big(\mathbf{\Omega} \times \mathbf{H}\big) = \mathbf{\Gamma}, \tag{3.35}$$

where $\mathbf{H}$ is the angular momentum vector, $\mathbf{\Omega}$ is the rotation vector and $\mathbf{\Gamma}$ is the torque external to the region considered. Taking the axial ($\hat{\mathbf{z}}$) component of equation (3.35), using $\mathbf{\Omega} = \Omega_z \hat{\mathbf{z}}$ and $H_z = C\Omega_z$, we find that $\mathbf{\Omega} \times \mathbf{H} = \mathbf{0}$ and (3.35) becomes

$$\frac{dH_z}{dt} = \frac{d}{dt}\big(C\Omega_z\big) = \Gamma. \tag{3.36}$$

Evaluating (3.36) for the mantle and inner core, respectively, gives

$$\frac{d}{dt} C_m \Omega_m = 2\overline{\Gamma}(\psi_s - \psi_m) \tag{3.37a}$$

$$\frac{d}{dt} C_s \Omega_s = -2\overline{\Gamma}(\psi_s - \psi_m), \tag{3.37b}$$

where equation (3.25) has been used, and the small angle approximation invoked, to provide the internal torque between the mantle and inner core. If we were to include magnetic, inertial, or viscous coupling, the angular momentum

budget would have to include the fluid core. By omitting these, angular momentum exchange is simplified and occurs only between the mantle and inner core.

The free-mode consists of the mantle and inner core oscillating about the equilibrium position with the free-mode frequency ω, hence we rewrite the terms $\Omega_{m,s}$ as periodic functions $\Omega_{m,s}e^{i\omega t}$. Subtracting (3.37b) from (3.37a) and taking a time derivative gives

$$\frac{d^2}{dt^2}\left[(C_m\Omega_m - C_s\Omega_s)e^{i\omega t}\right] = 4\overline{\Gamma}(\Omega_s - \Omega_m)e^{i\omega t} \tag{3.38}$$

where $\frac{d}{dt}\psi_{m,s} = \Omega_{m,s}$. Carrying out the differentiation reveals

$$-\omega^2(C_m\Omega_m - C_s\Omega_s) = 4\overline{\Gamma}(\Omega_s - \Omega_m). \tag{3.39}$$

This result can be simplified by eliminating $\Omega_{m,s}$ using a result which comes from adding (3.37a) and (3.37b),

$$\Omega_m = -\frac{C_s}{C_m}\Omega_s, \tag{3.40}$$

which expresses conservation of angular momentum between the mantle and inner core. Upon substitution of (3.40) into (3.39), we finally arrive at

$$\omega^2 C_s = 2\overline{\Gamma}\left(\frac{C_s + C_m}{C_m}\right), \tag{3.41}$$

which can be rearranged to show

$$\omega = \sqrt{\frac{2\overline{\Gamma}(C_m + C_s)}{C_s C_m}}. \tag{3.42}$$

The corresponding free-mode period is given by

$$T_{free} = \frac{2\pi}{\omega} = \sqrt{\frac{2\pi^2 C_s C_m}{\overline{\Gamma}(C_m + C_s)}}. \tag{3.43}$$

As expected, the period of the free-mode depends on the interplay between the magnitude of the gravitational couple and the polar moments of inertia of the mantle and inner core. Strong coupling (large $\overline{\Gamma}$) will tend to realign the inner core with the mantle more effectively if a misalignment is created between them. Large polar moments of inertia increase the difficulty with which changes in rotation rate can occur, and tend to lengthen the free-mode period. By exploring a range of interior structures, different combinations of $\overline{\Gamma}$ and $C_{m,s}$ will be used to evaluate T_{free}. If T_{free} approaches the 88 day period of the libration forcing, we can expect that this mode may be excited to a large amplitude and significantly participate in the libration response of Mercury. The gravitational free-mode is analysed further in chapter 5.

Chapter 4

Modelling Mercury's Rotation

4.1 Equations of Motion Governing Mercury's Rotation

The coupled differential equations that dictate the way Mercury rotates are well established. To determine the effects of an elliptical inner core on the librations of the mantle, we write two coupled equations for the libration of the mantle and inner core respectively (e.g. Danby, 1962)

$$C_m\ddot{\psi}_m + \frac{3}{2}(B_m - A_m)\frac{GM_\odot}{r_{orb}^3}\sin 2\delta_m = -\overline{\Gamma}\sin 2(\psi_m - \psi_s), \tag{4.1a}$$

$$C_s\ddot{\psi}_s + \alpha\frac{3}{2}(B_s - A_s)\frac{GM_\odot}{r_{orb}^3}\sin 2\delta_i = \overline{\Gamma}\sin 2(\psi_m - \psi_s) \tag{4.1b}$$

where $M_\odot$ denotes the Solar mass and $\ddot{\psi}_{m,s} \equiv \frac{d^2}{dt^2}\psi_{m,s}$. The term α is shorthand notation for the density contrast $1 - \frac{\rho_f}{\rho_s}$, r_{orb} is the Mercury-Sun distance and $\delta_{m,s}$ are the angles between the Mercury-Sun line and the axes of minimum moment of inertia of the mantle and inner core, respectively. From figure 4.1 it can be shown that $\delta_{m,s} = \psi_{m,s} - f$, where f is the angle that specifies Mercury's

position in its orbit around the Sun. The angle f is referred to as the *true free anomaly*. We write $\psi_{m,s} = \frac{3}{2}\mathcal{M} + \gamma_{m,s}$ with $\mathcal{M} = n(t - t_0)$ being the *mean anomaly of the orbital motion* such that $\frac{3}{2}\mathcal{M}$ represents Mercury's mean rotation and $\gamma_{m,s} = \delta_{m,s}$ when Mercury is at perihelion. The latter follows from the fact that Mercury's spin rate is $1.5n$, where $n = \frac{2\pi}{88 \text{ days}}$ is Mercury's orbital frequency. The term $\gamma_{m,s}$ now represents any perturbation in rotation from the mean rotation rate.

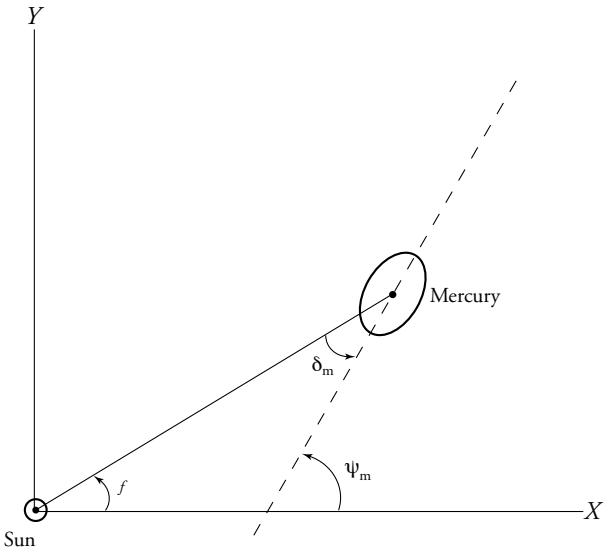

Figure 4.1: Angles used in libration discussion. Sun-X line is the Mercury-Sun line at perihelion. Dashed line marks the axis of minimum moment of inertia. For illustrative purposes, only angles pertaining to the mantle are shown. Figure adapted from Peale *et al.* (2007).

Substituting these definitions into (4.1a) and (4.1b) we find

$$C_m\ddot{\gamma}_m + \frac{3}{2}\Big(B_m - A_m\Big)\frac{GM_\odot}{r_{orb}^3}\sin\big(3n(t-t_0) + 2\gamma_m - 2f\big) = \overline{\Gamma}\sin 2(\gamma_m - \gamma_s), \tag{4.2a}$$

$$C_s\ddot{\gamma}_s + \alpha\frac{3}{2}\Big(B_s - A_s\Big)\frac{GM_\odot}{r_{orb}^3}\sin\big(3n(t-t_0) + 2\gamma_s - 2f\big) = \overline{\Gamma}\sin 2(\gamma_m - \gamma_s). \tag{4.2b}$$

We write r_{orb} in terms of the semi-major axis of Mercury's orbit a and the true free anomaly f, where

$$r_{orb} = \frac{a(1-e^2)}{1+e\cos f}.$$

Substituting this into equations (4.2a), (4.2b) and dividing through by $\frac{GM_\odot}{a^3} = n^2$ (a relation arising from the definition of the orbital period $T = 2\pi\sqrt{\frac{a^3}{GM_\odot}}$), reveals

$$\frac{\ddot{\gamma}_m}{n^2} = -\frac{3}{2}\Big(\frac{B_m - A_m}{C_m}\Big)\frac{(1+e\cos f)^3}{(1-e^2)^3}\sin\big(3n(t-t_0) + 2\gamma_m - 2f\big) - \frac{\overline{\Gamma}a^3}{GM_\odot C_m}\sin 2(\gamma_m - \gamma_s) \tag{4.3a}$$

and

$$\frac{\ddot{\gamma}_s}{n^2} = -\frac{3}{2}\alpha\Big(\frac{B_s - A_s}{C_s}\Big)\frac{(1+e\cos f)^3}{(1-e^2)^3}\sin\big(3n(t-t_0) + 2\gamma_s - 2f\big) - \frac{\overline{\Gamma}a^3}{GM_\odot C_s}\sin 2(\gamma_m - \gamma_s). \tag{4.3b}$$

Finally, we transform the variable t to the dimensionless nt so that an orbital period equals 2π and $\frac{1}{n^2}\frac{d^2\gamma_m}{dt^2} = \frac{d^2\gamma_m}{dt'}$ where $t' = nt$. Dropping the primes on t and taking $t_0 = 0$, we arrive at the set of differential equations

$$\ddot{\gamma}_m = -\frac{3}{2}\Big(\frac{B_m - A_m}{C_m}\Big)\frac{(1+e\cos f)^3}{(1-e^2)^3}\sin(3t + 2\gamma_m - 2f) - \frac{\overline{\Gamma}a^3}{GM_\odot C_m}\sin 2(\gamma_m - \gamma_s) \tag{4.4a}$$

and

$$\ddot{\gamma}_s = -\frac{3}{2}\alpha\Big(\frac{B_s - A_s}{C_s}\Big)\frac{(1+e\cos f)^3}{(1-e^2)^3}\sin(3t + 2\gamma_s - 2f) - \frac{\overline{\Gamma}a^3}{GM_\odot C_s}\sin 2(\gamma_m - \gamma_s). \tag{4.4b}$$

The final differential equation needed to solve for the spin rate $\dot{\gamma}_m$ is one that describes the rate of change of the true free anomaly with respect to time, given by

$$\dot{f} = \sqrt{\frac{1}{(1-e^2)^3}}(1 + e\cos f)^2, \tag{4.5}$$

and is derived from Kepler's second law. A full explanation of its origin is given in appendix A. In solving (4.4a), (4.4b) and (4.5), a set of initial conditions is required for $\gamma_{m,s}, \dot{\gamma}_{m,s}$ and f. Since observations of $\dot{\gamma}_m$ (Margot *et al.* 2007), with which we eventually want to make comparisons, are measured from perihelion, we automatically constrain the true free anomaly to be $f = 0$ at $t = 0$. There are effectively no restrictions on our choice of initial values for $\gamma_{m,s}$ or $\dot{\gamma}_{m,s}$, so they can take on non-zero values when $f = 0$, $t = 0$. One mechanism that arises from non-zero initial conditions is a *free libration*, which is an oscillation of ψ_m (or ψ_s) about the Mercury-Sun line at perihelion. The free libration should not be confused with the free-mode that occurs between the mantle and inner core. Peale *et al* (2002; 2005) expect that over time, any free libration of the mantle or inner core will be damped, which may be true if neither internal core convection nor mantle-inner core interaction are present. However, the possibility of convective core motion and the associated zonal flows are likely to couple electromagnetically with the inner core. This would represent a source of long term fluctuations in ψ_s and, by virtue of gravitational interaction, in ψ_m. Such internal dynamics are then likely to promote the misalignment of both ψ_m and ψ_s with the Mercury-Sun line at perihelion, and so we do not expect free librations to be damped out. Estimations of the period of the free librations can be made by dropping the coupling terms on the R.H.S of (4.4a) and (4.4b) and expanding $\sin(3t + 2\gamma_{m,s} - 2f)$, which gives rise to the factors $(a^3/r_{orb}^3)\sin 2f$ and $(a^3/r_{orb}^3)\cos 2f$. Expanding the two factors in terms of the mean anomaly $\mathcal{M}$ and using Cayley's (1859) tables

gives

$$\ddot{\gamma}_m + 3\Big(\frac{B_m - A_m}{C_m}\Big) H(p,e)\gamma_m = 0 \tag{4.6a}$$

and

$$\ddot{\gamma}_s + 3\alpha\Big(\frac{B_s - A_s}{C_s}\Big) H(p,e)\gamma_s = 0, \tag{4.6b}$$

for the mantle and inner core respectively, where $H(p,e)$ is a power series in eccentricity for a given resonance ratio p. For $p = \frac{3}{2}$ from Kaula (1966),

$$H(\frac{3}{2}, e) = \frac{7}{2}e - \frac{123}{16}e^3. \tag{4.7}$$

Solving the second order, linear differential equations given in (4.6a) and (4.6b) results in the well known solution for simple harmonic motion for both the mantle and inner core (e.g. Peale, 2007),

$$\omega_m = n\sqrt{3\frac{(B_m - A_m)}{C_m}\left(\frac{7}{2}e - \frac{123}{16}e^3\right)} \tag{4.8a}$$

and

$$\omega_s = n\sqrt{3\alpha\frac{(B_s - A_s)}{C_s}\left(\frac{7}{2}e - \frac{123}{16}e^3\right)} \tag{4.8b}$$

respectively. Estimating ω_m for an inertial ratio $\frac{B_m - A_m}{C_m} = 2.03 \times 10^{-4}$ (Margot *et al.* 2007) results in a free mantle libration period of 12.08 Earth years (50.1 orbital periods). The free libration period of the inner core depends on the chosen internal model of Mercury. These oscillations are likely participating in Mercury's spin rate, and their amplitude and phase are determined by the choices of initial conditions for $\gamma_{m,s}, \dot{\gamma}_{m,s}$. The mechanism for which the initial conditions are chosen is discussed in the following section.

4.2 Comparison Between Simulated and Observed Spin Rates

Solving the three differential equations (4.4a), (4.4b) and (4.5) provides the evolution of spin rate $\dot{\gamma}_m$ over time. In an attempt to find the interior structure that best represents Mercury's current configuration, it is necessary to compare the modeled solution for $\dot{\gamma}_m$ with spin rate observations. The comparison between simulated and observed spin rate data can be quantified using a residual technique. The residual is found using the method of least squares,

$$E^2 = (\mathbf{d} - \mathbf{p})^T \mathbf{C}_e^{-1} (\mathbf{d} - \mathbf{p}) \tag{4.9}$$

where

$$\mathbf{C}_e = \begin{pmatrix} \sigma_{11}^2 & 0 & \dots & 0 \\ 0 & \sigma_{22}^2 & \dots & 0 \\ \vdots & \vdots & \ddots & \vdots \\ 0 & 0 & \dots & \sigma_{NN}^2 \end{pmatrix}.$$

The *root mean square* (rms) residual E, is a measure of success of the model in fitting the data. A value of $E = 0$ would indicate a perfect fit. The terms $\mathbf{d}$ and $\mathbf{p}$ are one dimensional vectors comprising of spin rate observations and model predictions and are given by

$$\mathbf{d} = (d_1, d_2, \dots, d_N) \tag{4.10}$$

and

$$\mathbf{p} = (p_1, p_2, \dots, p_N), \tag{4.11}$$

respectively. Because the spin rate is an evolution in time, the indices on both vectors denote elapsed time from perihelion. The two dimensional covariance matrix $\mathbf{C}_e$ holds information on the standard deviation σ_{ij} of the observed spin rate measurements.

The observations of Mercury's spin rate and their respective standard deviations σ_{ij} are shown in table 4.1. The observations from Margot *et al.* (2007) give spin rates at specific times during Mercury's orbit. We compute predictions of spin rate at these specific times by integrating the set of differential equations (4.4a), (4.4b), (4.5) and evaluating them at each time for which there is an observation.

Table 4.1: Observations of $\dot{\gamma}_m$ from Margot *et al.* 2007. Spin rate is in units of 3/2 of the mean orbital frequency.

Date (yymmdd)	Spin rate	σ
020513	0.999985	1.61×10^{-5}
020522	0.999893	1.58×10^{-5}
020602	0.999861	1.69×10^{-5}
020612	0.999945	1.78×10^{-5}
030113	1.000097	1.37×10^{-5}
030123	1.000073	5.28×10^{-6}
030531	0.999932	8.21×10^{-6}
030601	0.999949	1.02×10^{-5}
030918	1.000093	5.03×10^{-5}
030919	1.000065	5.50×10^{-5}
030920	1.000067	5.18×10^{-5}
040331	1.000098	1.20×10^{-5}
041212	1.000070	1.55×10^{-5}
041218	1.000067	1.05×10^{-5}
041219	1.000075	9.67×10^{-6}
050313	1.000035	3.19×10^{-5}
050316	1.000047	1.45×10^{-5}
050318	1.000056	1.52×10^{-5}
060629	0.999866	8.35×10^{-6}
060712	0.999882	6.43×10^{-6}

All observations are mutually independent of one another, and the covari-

ance matrix is reduced to a diagonal one, with $\sigma_{ij} = 0$ for $i \neq j$. This simplifies the expression for the residual (4.9) to

$$E^2 = \sum_{i=1}^{N} \frac{(d_i - p_i)^2}{\sigma_{ii}^2}, \tag{4.12}$$

which has been written in index notation for clarity. This technique allows us to assess the behaviour of the residual E for a range of interior geometries, each of which is uniquely defined by the parameters χ_S^{in} and r_s. The existence of minima in E would suggest interior structures that are considered more probable representations of Mercury's current interior state.

In the previous section (4.1), we referred to our choice of initial conditions on $\gamma_{m,s}$ and $\dot{\gamma}_{m,s}$, and discussed how they were not constrained to definite values like the free anomaly f. Because of the large range of possible values for these conditions, we employ the *downhill simplex method* of Nelder & Mead (1965). For a given internal model structure, the simplex method searches for the set of initial conditions on $\gamma_{m,s}$ and $\dot{\gamma}_{m,s}$ that give the best fit to observations of $\dot{\gamma}_m$. A set of semi-random initial conditions is still required as input, and it is from these values that the simplex begins to converge on the set of optimal conditions that return minimum E. The reasoning for using semi-random and not fully-random initial conditions as input is primarily because it reduces computational time. This augmentation appears not to inhibit the process of finding optimal initial conditions because it is apparent from brief examination of spin-rate observations that the solution of $\dot{\gamma}_m$ with minimal E can only take on a limited range of suitable initial conditions. To ensure that the simplex is contracting around the minima of E, we repeat the convergence process five times, each with a different set of semi random initial conditions.

Chapter 5

Results and Discussion

In this section we attempt to relate changes in interior structure to changes in Mercury's spin rate. Our aim is not necessarily to determine how inner core growth affects the libration observations, but rather on trying to determine, using the libration, where the inner core is in its evolution. We begin this section by showing how the bulk properties of the planet are affected by inner core growth for a single core sulphur concentration. We then extend our results in an attempt to visualise how certain parameters vary as a function of both χ_S^{in} and r_s. Finally, we look at specific examples of simulated spin rates for different interior geometries, followed by a discussion on how estimations of libration amplitude are affected by including gravitational coupling between the mantle and inner core.

At first we look at density changes in the fluid core resulting from inner core growth. In all subsequent figures, we follow the growth of the inner core until the whole core is solidified; that is, until $r_s = r_f$. Figure 5.1 compares the evolution of outer core density for models with sulphur concentration $\chi_S^{in} = 0.05$ to the evolution of outer core density for models with no sulphur content.

For the case with no sulphur, the density contrast remains constant at α = 0.035 as a consequence of the 3.5% density difference between ρ_{Fe}^{solid} and ρ_{Fe}^{liquid}, along with the fluid core maintaining the density $\rho_{Fe}^{liquid} = 7874$ kg m^{-3} (as given in table 2.1) until it has solidified. For the case with sulphur, the increase in α is a response to the increasing concentration of sulphur in the fluid core as the inner core grows. Even for small inner core radii, the impact of sulphur on the density of the fluid core is very apparent, with α for the case with sulphur approximately twice as large as the case without. The change in α becomes greater with inner core radius, due to the increasing surface area available for the fluid core to precipitate on to. Beyond the eutectic radius, the composition of the fluid core does not change in sulphur concentration, resulting in a constant density contrast with $\alpha = 1 - \rho_f/\rho_s^{eut}$.

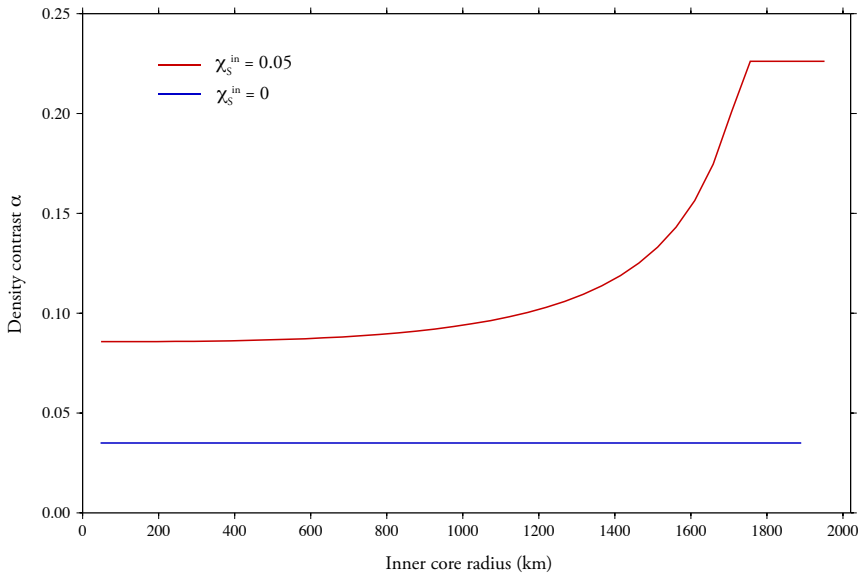

Figure 5.1: Comparison of density contrast $\alpha = 1 - \rho_f/\rho_s$ as a function of inner core radius r_s for different initial sulphur concentrations. Red line represents $\chi_S^{in} = 0.05$ while blue line is for a model with no sulphur.

Since the density contrast depends on both inner core radius and initial core sulphur concentration, we are able to present a more complete analysis by

plotting α as a function of both χ_S^{in} and r_s. Figure 5.2 shows a larger density contrast for models with higher sulphur concentrations, a result which is commensurate with the associated reduction in fluid core density that is incurred with high concentrations of sulphur. In the same fashion as in figure 5.1, α is maximum and its value remains constant beyond the eutectic radius. In figure 5.2 it is also apparent that the maximum density contrast that can be obtained is the same for all core sulphur concentrations, where $\alpha^{max} \sim 0.24$. This result comes from the fact that the eutectic composition of $\chi_{FeS}^{eut} = 0.61$ (section 2.3) is independent of initial core sulphur concentration. Substituting this value of eutectic composition into equation (2.5) and using it in the definition of α returns the upper limit $\alpha^{max} \sim 0.24$.

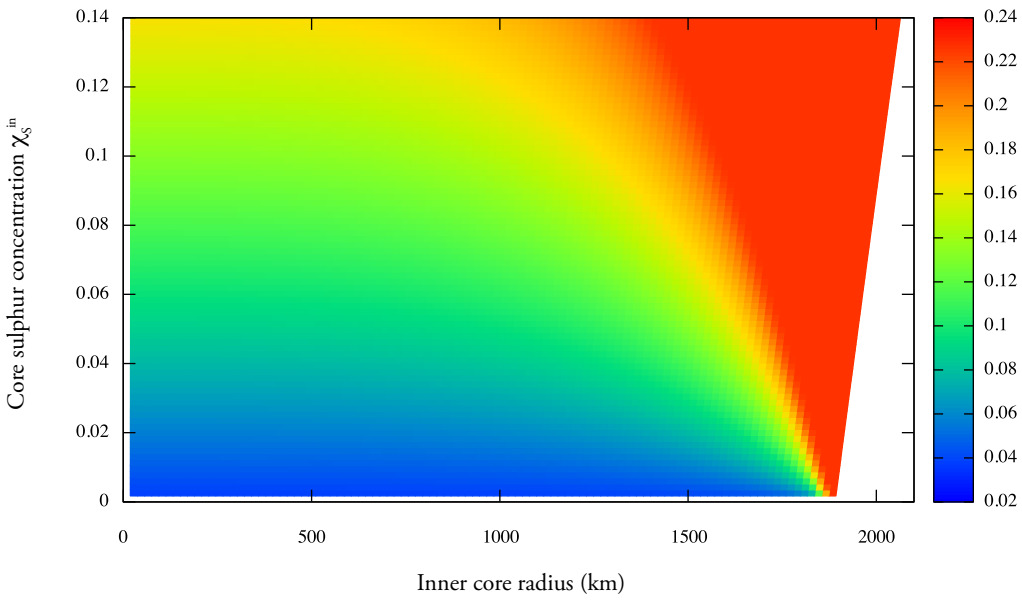

Figure 5.2: Density contrast α as a function of initial core sulphur concentration and inner core radius.

Other factors which are influenced by inner core growth are the polar mo-

ments of inertia of the mantle C_m, fluid core C_f and inner core C_s. Figure 5.3 demonstrates the change in moments of inertia for the mantle, fluid and inner cores. Here we have normalised C_m, C_f and C_s with the planetary moment of inertia C. The moment of inertia of the mantle, C_m remains constant as the inner core grows because there is no change in mantle density and, for a given χ_S^{in}, no change in r_f and hence, no change in mantle thickness. The same is not true for the inner core, which shows an increase in C_s purely because of the increase in its radius.

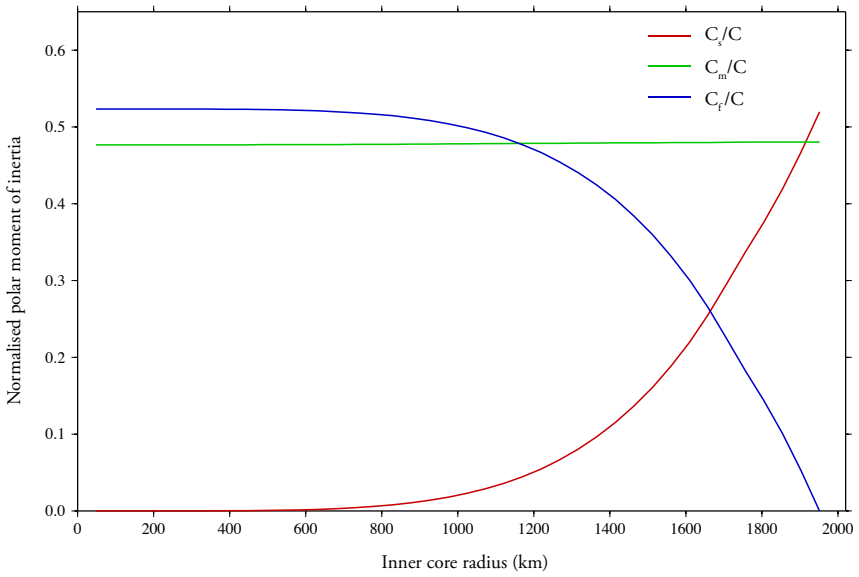

Figure 5.3: Evolution of polar moments C_m (green), C_f (blue) and C_s (red) as inner core grows. All values are normalised by the planetary polar moment C. Example shown is for $\chi_S^{in} = 0.05$.

As the inner core radius increases, the fluid core diminishes in both density and thickness. The combined effect causes a reduction in C_f. Beyond the eutectic radius, the decrease in fluid core density no longer occurs, and only the continuous decrease in fluid core thickness contributes to the reduction in C_f. The differences in the two regimes that occur before and after the eutectic radius is noticeably small, but can be seen in figure 5.3 at the eutectic radius

$r_s^{eut} = 1740$ km. A similar change is seen in the C_s curve, but is caused by the thin layer of material of density ρ_s^{eut} on top of the solid iron core which is introduced beyond r_s^{eut}. The apparent anti-symmetry between C_s and C_f indicates that the normalised change in polar moment of inertia for the whole core C_{core}/C remains constant as the inner core increases in radius. However, upon closer inspection it can be shown that the moment of inertia for the whole core decreases (figure 5.4).

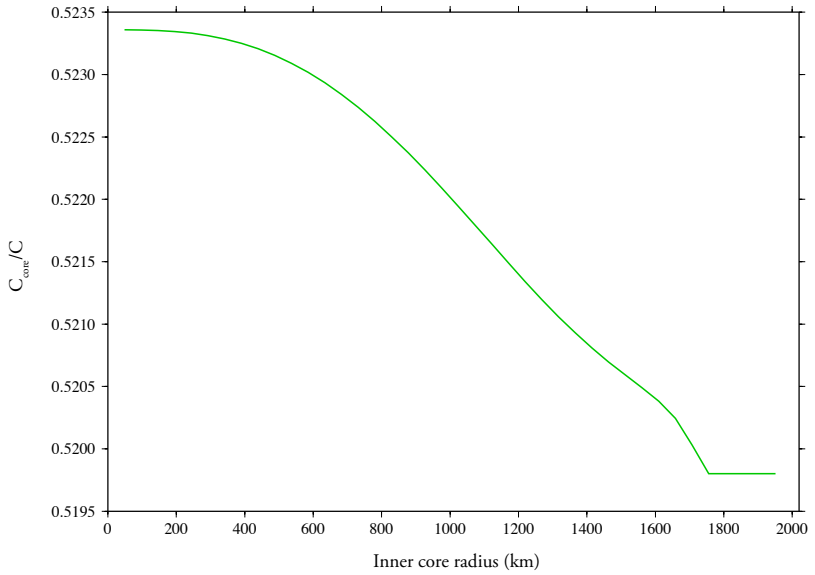

Figure 5.4: Evolution of normalised polar moment of the entire core ($C_s/C + C_f/C$).

This can be reconciled with the redistribution of mass inside the core that arises upon precipitation of the inner core. Initially, when the core is entirely fluid, the distribution of mass is assumed to be homogeneous. The solidification of an inner core, which exhibits a greater density than the initial fluid core, creates a geometry where mass is concentrated toward the planet centre. After the eutectic limit has been reached, the geometry consists of a dense inner core, with an overlaying, less dense layer. The excursion from core homogeneity to heterogeneity is responsible for the decrease in core inertia.

5.1 Shape of the Mantle, CMB and Core

The ellipticities of the mantle, CMB and core are important considerations if the model is to conform to observations of C_{22} and $\Delta\gamma_m$. In this section, we look at changes in the equatorial ellipticity of the mantle, CMB and entire core as the inner core grows.

Figure 5.5 shows curves of ϵ_m, ϵ_f and ϵ_i as a function of inner core growth for the core sulphur concentration $\chi_S^{in} = 0.05$. The quantities ϵ_m and ϵ_f show similar characteristics. Both exhibit a sharp decline after an initial, approximately constant regime. The decreases in ϵ_m and ϵ_f are responses to the inner core becoming closer to both the CMB and Mercury's surface as the inner core radius increases. As the mass inside the inner core boundary encroaches on the latter two density discontinuities, the inner core makes a greater contribution to the gravitational potential at both the CMB and Mercury's surface, and hence a greater contribution to the C_{22} coefficient (which is measured at a point external to Mercury's surface). The relatively high density of the inner core means that it also provides a larger contribution to gravitational potential than, for example, a body with similar dimensions but smaller density. If there were no compensation for the increased gravitational potential (as measured at Mercury's surface) caused by the increasing contribution from the inner core, the magnitude of the C_{22} coefficient of the model would be elevated above the current observed value and the model no longer consistent with observations. To accommodate for the increase in C_{22}, a decrease in the ellipticity of the mantle and CMB occurs, which in turn reduces the contribution to C_{22} so that the observed value is not violated.

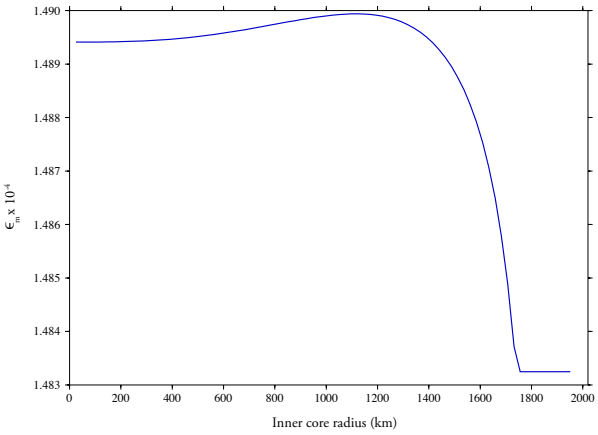

(a)

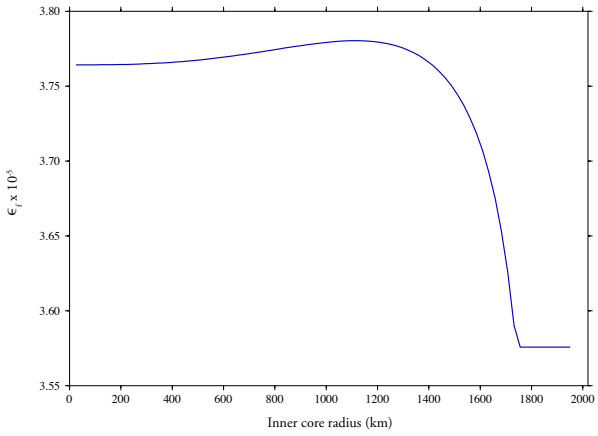

(b)

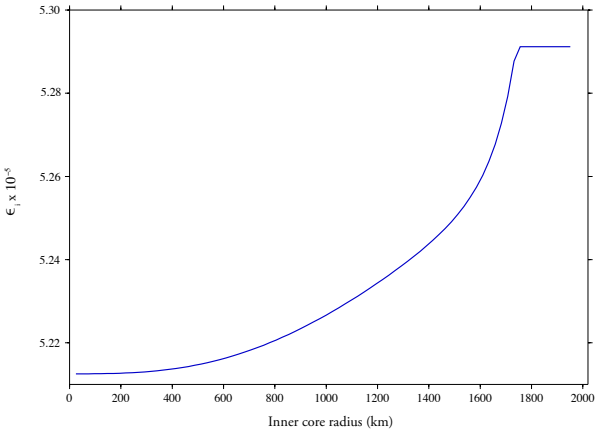

(c)

Figure 5.5: Equatorial ellipticity of (a) the mantle ϵ_m, (b) core-mantle boundary ϵ_f and (c) core ϵ_i as a function of inner core radius. All results for $\chi_S^{in} = 0.05$.

The constant values that are exhibited by ϵ_m and ϵ_f beyond the eutectic radius can be easily explained; both factors are obtained from observations of C_{22} and $\Delta\gamma_m$, but the variables that contribute to these expressions no longer change when $r_s > r_s^{eut}$ (see equations (B.5) and (B.6)). In other words, C_{22} and $\Delta\gamma_m$ do not change beyond r_s^{eut}. The increase in the ellipticity of the core $\epsilon_i = k_m\epsilon_m + k_f\epsilon_f$ with inner core radius can be attributed to the factor k_m, since all other terms in the expression for ϵ_i tend to decrease with inner core growth. In figure 5.6 both factors k_m and k_f are plotted versus r_s. The decrease in ρ_f associated with inner core growth invokes an increase in k_m, and is the reason for the increase in ϵ_i seen in figure 5.5c. The constant value of ϵ_i for $r_s > r_s^{eut}$ can be attributed to the constant values of k_m and k_f, which in turn follow on from the fact that ρ_f is constant beyond the eutectic radius.

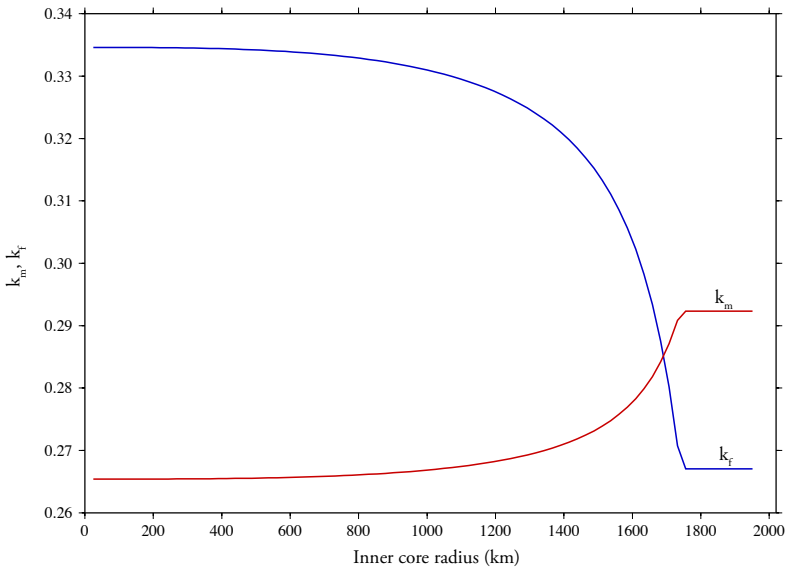

Figure 5.6: Factors k_m (red) and k_f (blue) versus inner core radius for $\chi_S^{in} = 0.05$.

5.2 Torque Magnitude and Free-Mode Period

The expectation that the gravitational coupling constant $\overline{\Gamma}$ should be approximately proportional to C_s (see equation 3.34) is largely consistent with the numerical predictions in figure 5.7. The coupling between the mantle and inner core is strongest when the thickness of the decoupling fluid core is smallest, or in other words, when the inner core radius is largest. Beyond the eutectic radius, the magnitude of $\overline{\Gamma}$ remains constant since only the redistribution of homogeneous material of the same density occurs after this point. However, this would not be the case for $\overline{\Gamma}$ if we were to account for the 3.5% density difference due to the phase change of Fe and FeS (see appendix B).

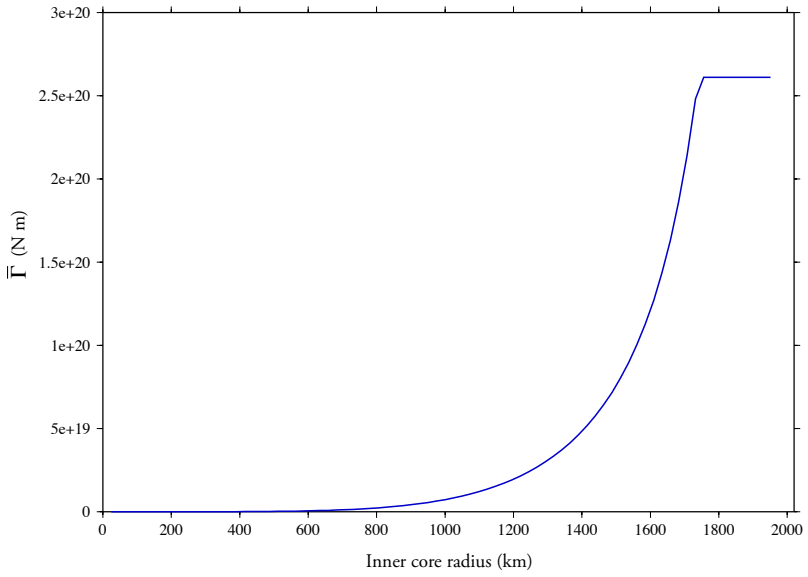

Figure 5.7: Magnitude of gravitational coupling constant $\overline{\Gamma}$ as a function of r_s. Curve is for $\chi_S^{in} = 0.05$.

Since the radii of the CMB and the eutectic boundary change with core sulphur concentration, along with density contrasts between the mantle, inner and outer cores, we also assess how the coupling constant changes with χ_S^{in}.

The surface plot seen in figure 5.8 shows the magnitude of $\overline{\Gamma}$ as a function of both χ_S^{in} and r_s. For illustrative purposes, $\overline{\Gamma}$ has been plotted using a logarithmic scale. The magnitude of the couple has little dependence on core sulphur concentration; it is inner core radius that is the controlling factor. As mentioned above, this is an expected result since our expression for torque (3.34) shows that $\overline{\Gamma} \propto C_s \propto r_s^5$ for $r_s < r_s^{eut}$, whereas only the density terms are affected by changes in χ_S^{in}.

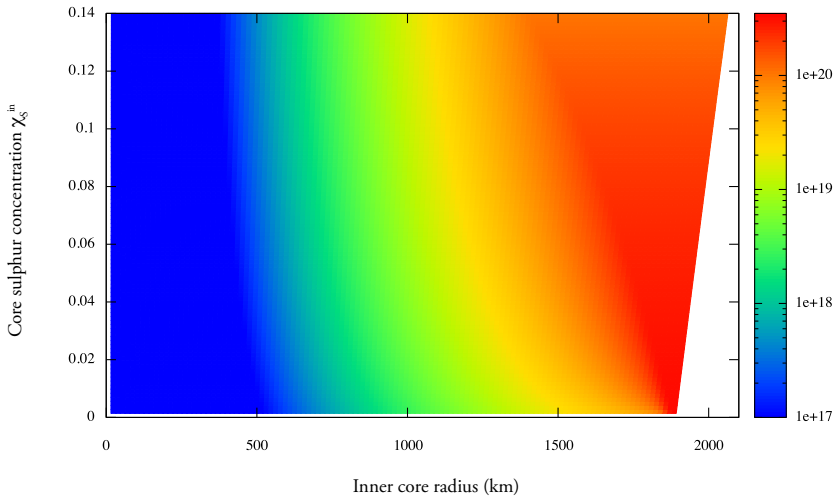

Figure 5.8: Two dimensional surface plot representation of $\overline{\Gamma}$ (Nm) as a function of χ_S^{in} and r_s.

The corresponding period of the associated free-mode between the mantle and inner core T_{free} is plotted first in one dimension (figure 5.9). Again, the curve is shown for a sulphur concentration of $\chi_S^{in} = 0.05$. The general trend shows a decrease in period with increasing r_s. This is mainly a consequence of stronger gravitational coupling between the mantle and inner core, which locks the inner core to the mantle more efficiently. The period of the free-mode is minimum at the eutectic radius, beyond which the period begins to lengthen. The reason for this reversal is due to the fact that $\overline{\Gamma}$ does not grow

beyond the eutectic limit, whereas the polar moment of inertia for the inner core continues to increase, thus impeding changes in rotation rate and reducing the effectiveness of the coupling.

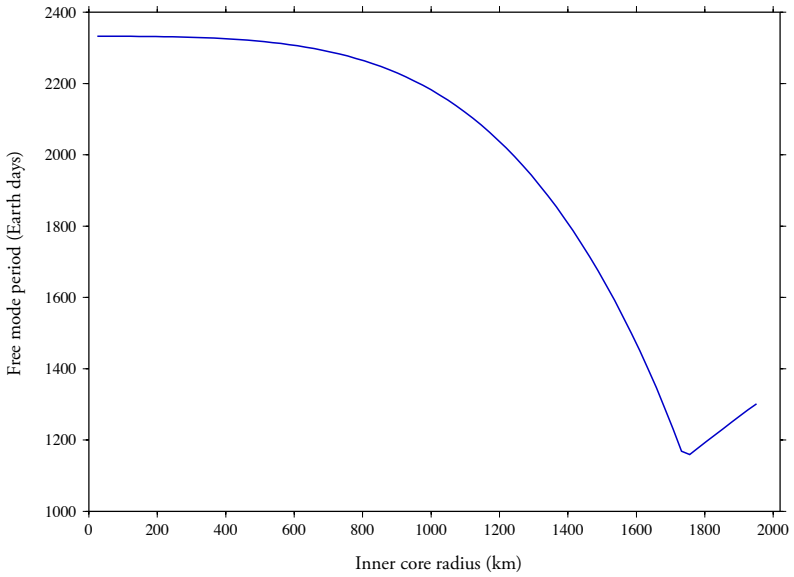

Figure 5.9: Free-mode period versus inner core radius for $\chi_S^{in} = 0.05$.

In a similar fashion to our illustration of $\overline{\Gamma}$, we also present the free-mode period T_{free} as a function of both χ_S^{in} and r_s (figure 5.10) . In comparison to $\overline{\Gamma}$, T_{free} has less of a dependence on the inner core radius, and is relatively more susceptible to changes in core sulphur concentration. The contrast in functional dependence on inner core radius becomes evident in the expression for the free-mode period (3.43), in which $T_{free} \propto \sqrt{\frac{1}{C_s}} \propto r_s^{-5/2}$ in comparison to $\overline{\Gamma} \propto C_s \propto r_s^5$ for $r_s < r_s^{eut}$. The sharp minimum in the period is shown clearly in figure 5.10, with T_{free} establishing periods as low as 1000 Earth days ($\simeq 11$ orbital periods). The minima occur at progressively smaller inner core radii as the sulphur concentration increases; this is a consequence of the eutectic radius r_s^{eut} becoming smaller with increasing χ_S^{in}. Beyond r_s^{eut} in models with high concentrations of sulphur, we also observe the increase in T_{free} that was

exemplified in figure 5.9.

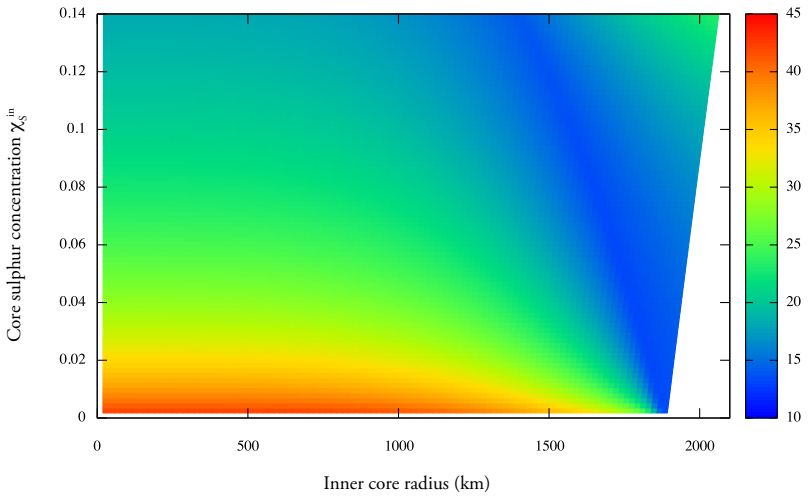

Figure 5.10: Two dimensional surface plot representation of free-mode period T_{free} in orbital periods as a function of χ_S^{in} and r_s.

5.3 Free Libration of the Mantle and Inner Core

As mentioned in section 4.1, the free mantle libration period has a constant value of 50.1 orbital periods for an inertial ratio of $\frac{B_m - A_m}{C_m} = 2.03 \times 10^{-4}$. However, the free libration period of the inner core is dependent on the density contrast α and the inertial ratio of the inner core $\frac{B_s - A_s}{C_s}$, so the libration period of the inner core is expected to change with the model parameters r_s and χ_S^{in}. Figure 5.11 shows the magnitude of the free libration period of the inner core as a function of χ_S^{in} and r_s. The free libration period ranges from 150 to 550 orbital periods. As expected, the libration period is longest for small inner core radii (small $\frac{B_s - A_s}{C_s}$) and low sulphur concentrations (small α).

The converse is true for short libration periods. However, even the shortest periods are approximately three times as long the free libration period of the mantle. Based on these values, we do not expect the inner core free libration to participate significantly in the mantle's forced libration period of 88 days.

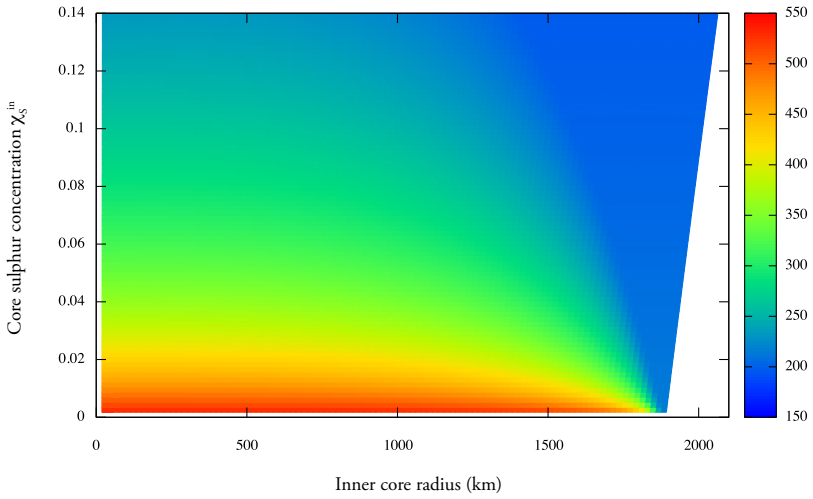

Figure 5.11: Two dimensional surface plot representation of the free libration of the inner core, measured in orbital periods, as a function of χ_S^{in} and r_s.

5.4 Misfit

The preceding results have been used to lead up to the most significant part of this study, in which a direct comparison between modeled and observed spin rate data is conducted. After calculating all the necessary parameters that are prerequisite for solving the set of equations governing Mercury's rotation, we are now able to discuss the impact of the free-mode oscillation on Mercury's spin rate, and determine the most probable model representation of Mercury's current state. Figure 5.12 shows the misfit between modeled libration curves

and spin rate observations as a function of χ_S^{in} and r_s; smaller misfit values indicating better fits to the observations. The most conclusive feature of figure 5.12 is the relatively poorer fit to observations with inner core radii less than 500 km. Misfit values in this region are on the order of $\sim$ 1.05. For $r_s > 500$ km, there is little variation in misfit in both inner core radius and sulphur concentration, with almost all misfit values falling between 0.7 and 0.85. The region of r_s at the eutectic radii exhibits a slightly increased misfit value due to the high free-mode frequency. Beyond the eutectic radius, the misfit begins to decrease as a result of the lengthening period of the free-mode.

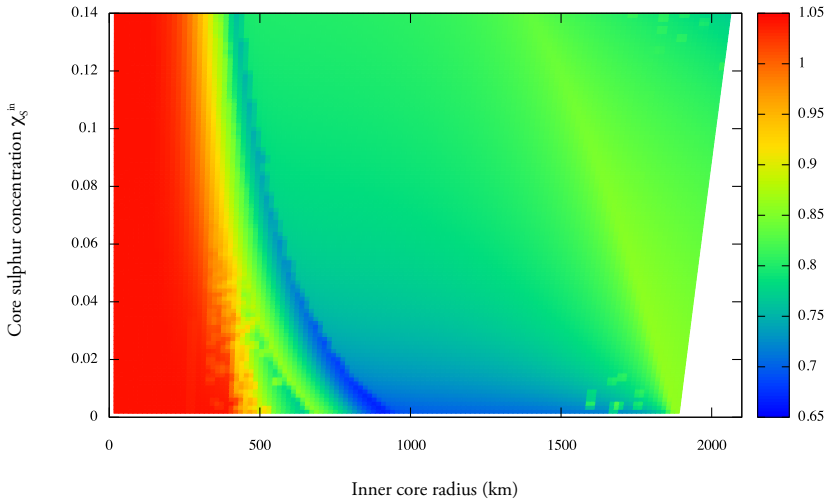

Figure 5.12: Misfit between modeled and observed spin rate data plotted against χ_S^{in} and r_s.

The region showing the smallest misfit of $\sim$ 0.7 occurs where $r_s \sim 900 - 1500$ km and χ_S^{in} = 0-0.02. Despite the marginally smaller misfit, it would be highly presumptuous to conclude that Mercury's current interior structure was distinguished by these exact parameters. A more prudent argument suggests that the results show a preferred inner core radius greater than $\sim$500 km, but

the invariance of the misfit with respect to χ_S^{in} reveals no information on the chemical composition of the core.

To elucidate the results encapsulated in figure 5.12, two values of inner core radii and core sulphur concentrations have been chosen to demonstrate two extremities of misfit. The associated modeled spin rate solutions of the mantle $\dot{\gamma}_m$ are shown in figure 5.13 with the mean rotation rate removed, thus representing spin rate deviations from the mean rotation rate. The spin rate evolutions shown are the best possible fit to observations for a given combination of χ_S^{in} and r_s, where the optimum initial conditions on $\gamma_{m,s}$ and $\dot{\gamma}_{m,s}$ are found from the Nelder & Mead (1965) minimisation scheme discussed in section 4.2. The observed spin rate values from Margot *et al.* (2007) are also plotted in figure 5.13 as points measured from the perihelion passage on April 17$^{\text{th}}$ 2002.

The complex behaviour of Mercury's spin rate at perihelion has been described by Peale (2005). In figure 5.13a, there exists a local minima in $\dot{\gamma}_m(t)$ at perihelion, with two local maxima before and after perihelion, corresponding to the planet's axis of minimum moment of inertia (the long axis) being aligned with the Mercury-Sun line. We ignore the variation in rotation due to the physical librations in determining the torque on Mercury by assuming the planet is rotating uniformly with $\dot{\psi}_m = 1.5n$. At perihelion, the long axis is also pointing toward the Sun, but $\dot{f} > \dot{\psi}_m = 1.5n$ at this point in the orbit. The long axis lags behind the motion of the Sun with respect to Mercury as the planet passes perihelion, and therefore starts to point away from the Sun in the direction of the orbital motion. The angle between the Sun and the long axis continues to grow until it reaches a local maximum when $\dot{f} = \dot{\psi}_m$. The torque on Mercury during this time increases the angular velocity, corresponding to the increase in $\dot{\psi}_m$ with time just after passing the point of perihelion.

The increase in $\dot{\psi}_m$ with time experiences an inflection and starts to decrease after the point in time when $\dot{f} = \dot{\psi}_m$, which corresponds to the time at which the angle between the long axis and the Sun starts to decrease. To bring the planet's long axis back into alignment with the Sun after passing the point of perihelion, Mercury must rotate through the same angle as it has moved in its orbit. Once this occurs, the long axis is ahead of the motion of the Sun with respect to Mercury, and the angular velocity starts to decrease. Mercury is almost synchronously rotating with its instantaneous orbital motion near the point of perihelion, during which time the long axis never deviates much from pointing toward the Sun. Therefore, $\dot{\psi}_m$ is nearly constant for a time near perihelion, as seen in figure 5.13a.

In figure 5.13a we have chosen values of $\chi_S^{in} = 0.02$ and $r_s = 100$ km that are commensurate with a large misfit value (~ 1.05). The resulting solution to $\dot{\gamma}_m$ in 5.13a shows the 88 day period forced libration superimposed on to a much longer period oscillation. The long period oscillation is a combination of the excitation of 50 orbital period free libration of the mantle and the mantle-inner core free-mode. The free libration period of the inner core is too long at 420 orbital periods, to be observed. Although the period of the long oscillation cannot be seen fully, figure 5.13a shows a half period of approximately 25 orbital periods, corresponding to an estimated full period on the order of 50 Mercurian orbits. A numerical evaluation of the gravitational free-mode for $\chi_S^{in} = 0.02$, $r_s = 100$ km gives a value of $T_{free} \sim 35$ orbital periods. This shows that for this given choice of χ_S^{in} and r_s, the best fit to observations is obtained with a free-mode period which is not excited and a long period oscillation dominated by the free libration of the mantle alone.

In comparison to 5.13a, 5.13b demonstrates the evolution of spin rate for a model with a combination of $\chi_S^{in} = 0.02$, $r_s = 900$ km that exhibits a

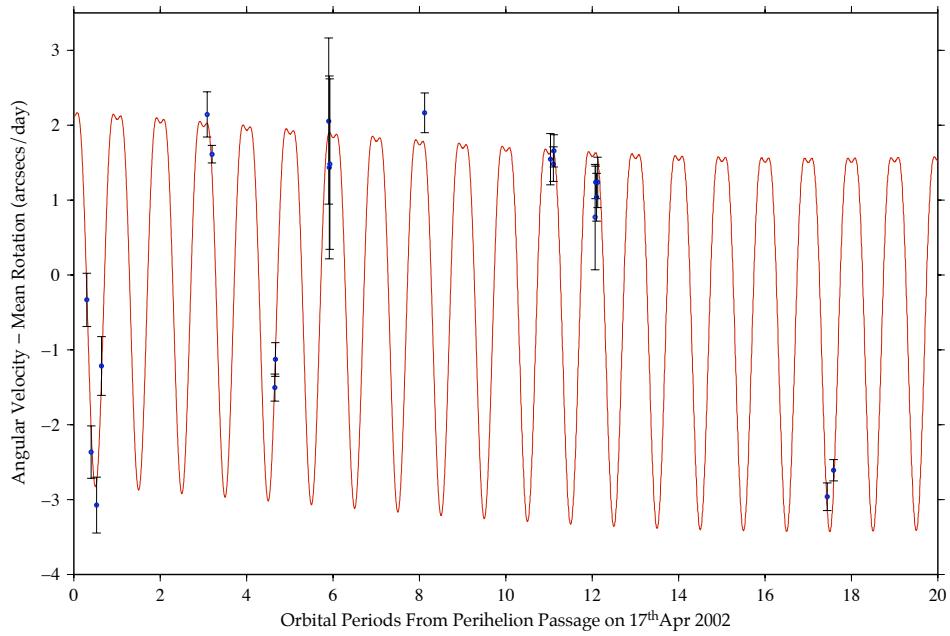

(a)

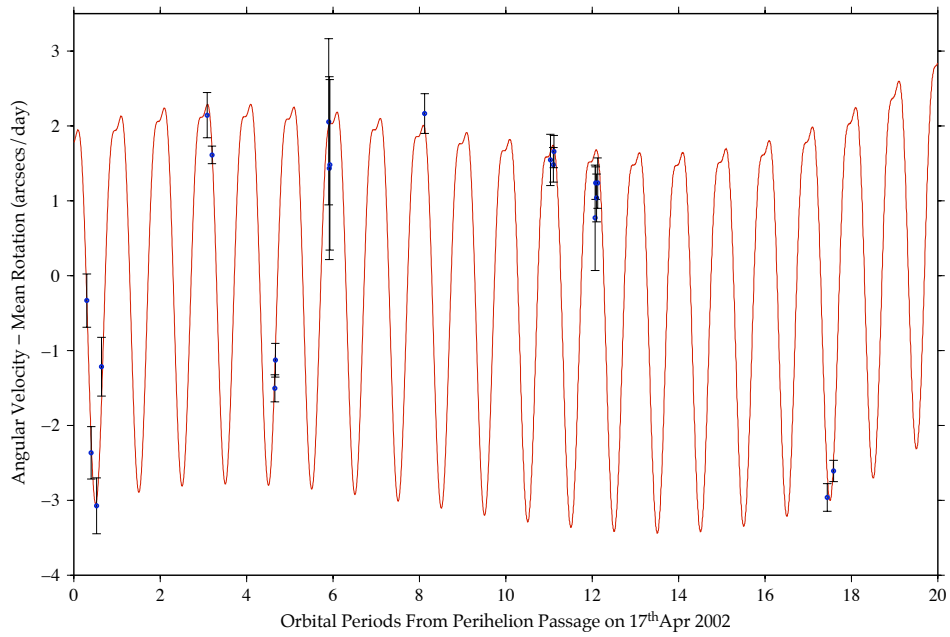

(b)

Figure 5.13: (a) Example of spin rate deviation from mean rotation rate $\dot{\gamma}_m(t)$ shown by red curve for $\chi_S^{in} = 0.02$, $r_s = 100$ km. Blue points are spin rate observations with standard deviation, from Margot *et al.* (2007). (b) Same as (a) but with $\chi_S^{in} = 0.02$, $r_s = 900$ km.

relatively small misfit of ~ 0.73 (see figure 5.12). It is clear from 5.13b that the 88 day forced libration is also superposed on to a relatively long (i.e. longer than 88 days) period oscillation. However, unlike in figure 5.13a, the gravitational free-mode between the mantle and inner core is more excited. The observed half-period in figure 5.13b is approximately 10 orbital periods, revealing a full period of 20 orbital periods. However, this observed period is shorter than both the calculated free-mode period of $T_{free} \sim 30$ orbital periods and the free mantle libration of 50 orbital periods. The observed 20 orbital period oscillation can be explained by looking at the beat periods (T_1, T_2) resulting from the interaction between the gravitational free-mode (T_{free}) and free mantle libration (T_{lib}). The beat periods are given by

$$T_1 = \frac{2\pi}{\left(\frac{2\pi}{T_{free}} - \frac{2\pi}{T_{lib}}\right)} = \frac{1}{\left(\frac{1}{T_{free}} - \frac{1}{T_{lib}}\right)} = 75 \text{ orbital periods}, \tag{5.1a}$$

$$T_2 = \frac{2\pi}{\left(\frac{2\pi}{T_{free}} + \frac{2\pi}{T_{lib}}\right)} = \frac{1}{\left(\frac{1}{T_{free}} + \frac{1}{T_{lib}}\right)} = 19 \text{ orbital periods}. \tag{5.1b}$$

The observed oscillation in figure 5.13b represents the beat period T_2, indicating that both the free mantle libration and gravitational free-mode are present. Although the difference in fitting $\dot{\gamma}_m$ to observations in the two scenarios is more discernible in figure 5.12, it is still apparent without pursuing a numerical quantification of misfit. By including the gravitational interaction between the mantle and inner core, we provide an extra parameter with which the observations can be fit. The extent to which the extra parameter can be used to fit the data is limited by the interior structure of the model as defined by χ_S^{in}, r_s, but at inner core radii greater than $r_s > 500$ km, the period of the free-mode appears to be short enough to enable a marginally better fit, although for some interior geometries it remains possible for the period to be too short and inhibit the fit to observations. Unfortunately, our results are not

able to constrain more precisely the present radius of the inner core. However, it is interesting to note that our results are also consistent with an inner core radius of ~ 1000 km, which can be inferred from the estimated 3 km decrease in the planetary radius (see figures 2.3 and 2.4).

Even if new observations of Mercury's global magnetic field confirm the existence of an internal dynamo, our constraint that $r_s \gtrsim 500$ km cannot distinguish between thick and thin (fluid) shell dynamo regimes. However, numerical dynamo models have shown that the magnetic field signatures of thick and thin shell geometries exhibit different characteristics, such as field partitioning between poloidal and toroidal components, and the latitude of flux bundles (e.g. Heimpel *et al.* 2005; Stanley *et al.* 2005; Christensen, 2006). Hence, new magnetic field observations from Messenger and BepiColombo should be able to infer the core geometry in which Mercury's dynamo is operating, and in the near future it is anticipated that more independent estimations or constraints on the radius of the inner core will be available.

5.5 Revising the Libration Amplitude

Throughout this study we have adopted the moment of inertia ratio $\Delta\gamma_m = \frac{B_m - A_m}{C_m}$ given by Margot *et al.* (2007), who measured $\Delta\gamma_m = (2.03 \pm 0.04) \times 10^{-4}$. The aim of this section is to investigate whether the inclusion of mantle-inner core gravitational coupling will reveal an optimal moment of inertia ratio that differs from that of Margot *et al.* (2007). We do not treat $\Delta\gamma_m$ as a parameter to be optimised, but rather repeat the analysis of the previous section for a range of values of $\Delta\gamma_m$. Figure 5.14 shows misfit plots for a range of inertial ratios between $\Delta\gamma_m = 1.99 \times 10^{-4}$ and $\Delta\gamma_m = 2.26 \times 10^{-4}$. All plots use the same colour scale for comparative purposes. Figure 5.14b uses Margot's estimated libration amplitude of $\Delta\gamma_m = 2.03 \times 10^{-4}$, and is used a basis for comparison. The changes in libration amplitude induce subtle changes in the magnitude of the misfit, although the contours of the plots are similar. The fact that the general shape of the misfit plot does not change significantly suggests that this method is sufficient to extract the optimal value of $\Delta\gamma_m$. The pixellation that can be seen in figures 5.14f to 5.14h is a result of non-convergence to the minimum E, and is a consequence of the downhill simplex method (discussed in section 4.2).

It is surprising to note that plot 5.14b (for which $\Delta\gamma_m = 2.03 \times 10^{-4}$) does not represent the optimal amplitude with the smallest misfit magnitudes. Increasing the libration amplitude to approximately $\Delta\gamma_m = 2.19 \times 10^{-4}$ in figure 5.14f provides the best fit to observations of Mercury's rotation rate. A further increase in the amplitude beyond $\Delta\gamma_m = 2.19 \times 10^{-4}$ illustrates a general increase in misfit magnitude, suggesting that the amplitude is too large to provide an optimal fit.

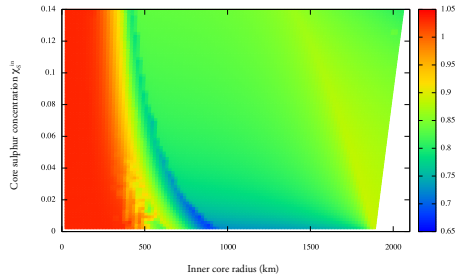

(a) $\Delta\gamma_m = 1.99 \times 10^{-4}$

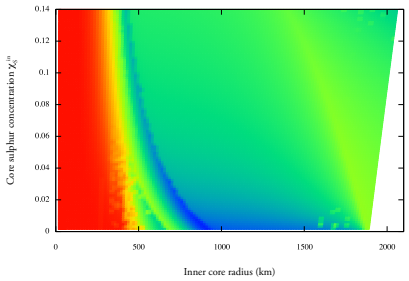

(b) $\Delta\gamma_m = 2.03 \times 10^{-4}$

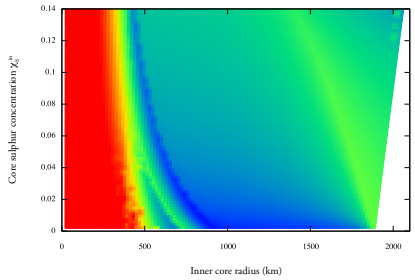

(c) $\Delta\gamma_m = 2.07 \times 10^{-4}$

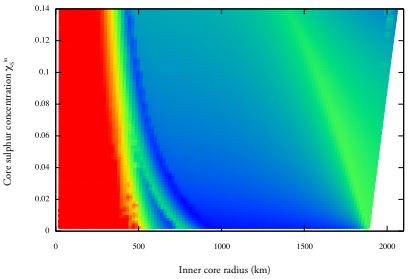

(d) $\Delta\gamma_m = 2.11 \times 10^{-4}$

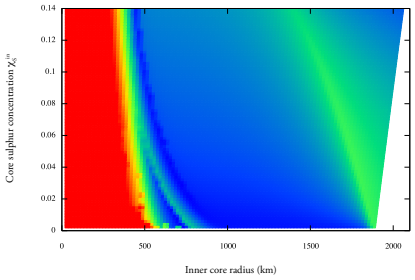

(e) $\Delta\gamma_m = 2.15 \times 10^{-4}$

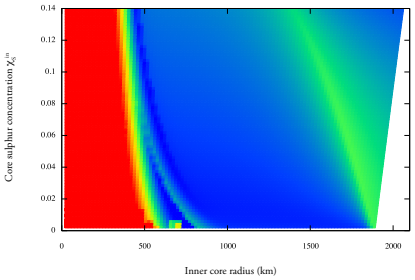

(f) $\Delta\gamma_m = 2.19 \times 10^{-4}$

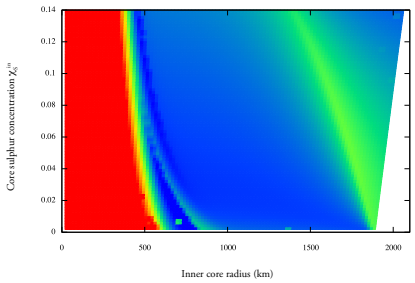

(g) $\Delta\gamma_m = 2.23 \times 10^{-4}$

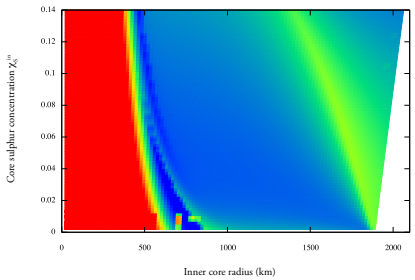

(h) $\Delta\gamma_m = 2.27 \times 10^{-4}$

Figure 5.14: Misfit for range of libration amplitudes.

In order to refine the value of $\Delta\gamma_m$ which provides the best fit to observations, the iteration process has been repeated for $2.16 \leq \Delta\gamma_m \leq 2.22$ in increments of 0.01 (figure 5.15). It becomes nearly impossible to observe any discernible differences in any of the plots from $\Delta\gamma_m = 2.19 \times 10^{-4}$. It is therefore reasonable to keep the previously stated $\Delta\gamma_m = 2.19 \times 10^{-4}$ as the preferred value for the moment of inertia ratio. One of the residing difficulties in finding the optimum moment of inertia ratio is that for a given combination of χ_S^{in} and r_s, the same misfit value might be obtained for a range of moment of inertia ratios. For example, the misfit value in figure 5.14b ($\Delta\gamma_m = 2.03 \times 10^{-4}$) for $\chi_S^{in} = 0.01$ and $r_s = 900$ km is approximately the same as that found in figure 5.14f ($\Delta\gamma_m = 2.19 \times 10^{-4}$) for the same model parameters. Therefore, a more diligent argument would conclude that there is a higher probability of finding a smaller misfit with the optimal moment of inertia ratio $\Delta\gamma_m = 2.19 \times 10^{-4}$, although the uncertainty on this value is likely to be of the order $\pm 0.1 \times 10^{-4}$.

The implication of obtaining an moment of inertia ratio larger than that found by Margot *et al.* (2007) is that the libration amplitude might be larger than previously acknowledged (38.6 arc sec compared to 35.8 arc sec), although this hypothesis cannot be tested until more observations have been collected by Messenger and BepiColombo. The discrepancy between these two values is not solely due to the inclusion of gravitational interactions within our model. It is also because the model used in this study considers the ellipticity of material surfaces throughout the whole planet, and is therefore fully consistent with measurements of the C_{22} harmonic coefficient. In contrast, Margot *et al.* (2007) implicitly assumed a spherical fluid core for which $B_m - A_m = B - A$. This represents a significant difference between the two models.

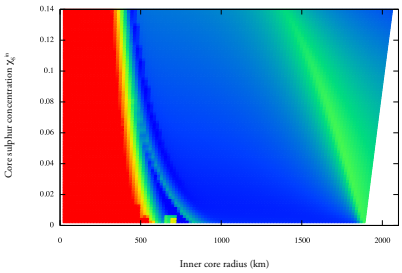

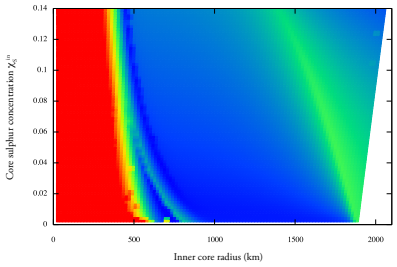

(a) $\Delta\gamma_m = 2.16 \times 10^{-4}$

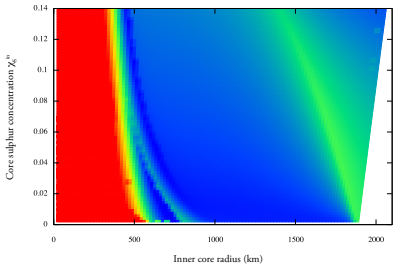

(b) $\Delta\gamma_m = 2.17 \times 10^{-4}$

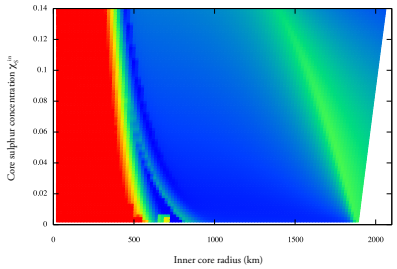

(c) $\Delta\gamma_m = 2.18 \times 10^{-4}$

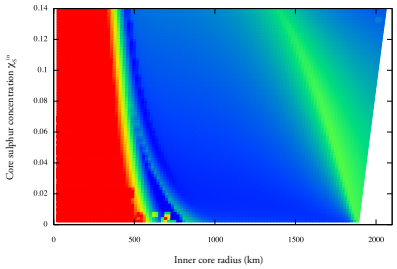

(d) $\Delta\gamma_m = 2.20 \times 10^{-4}$

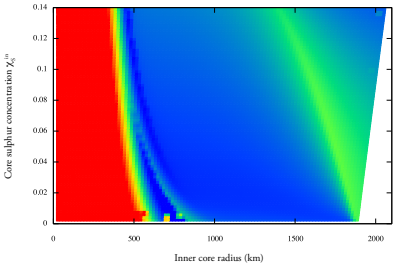

(e) $\Delta\gamma_m = 2.21 \times 10^{-4}$

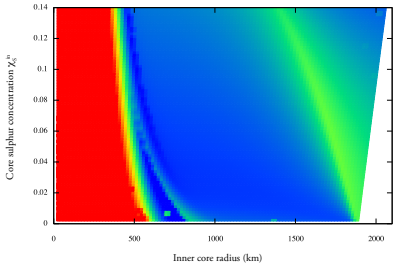

(f) $\Delta\gamma_m = 2.22 \times 10^{-4}$

Figure 5.15: Misfit for range of refined libration amplitudes. Top figure shows misfit for $\Delta\gamma_m = 2.19 \times 10^{-4}$ and is for comparison purposes.

Chapter 6

Summary and Future Outlook

It has been shown that by including gravitational interaction between the mantle and inner core, we are able to generate a mode of oscillation which, in the case of strong coupling is significant enough to improve the fit between the modeled and observed spin rate variations of Mercury. However, in the case of some model geometries, the free-mode period is too short and is not able to improve the fit to observed spin rate variations. This suggests that gravitational inner core-mantle coupling participates in Mercury's librations. Despite quantifying the residual between model and observations for a range of plausible interior geometries, we are unable to obtain a precise combination of inner core radius and core sulphur concentration that presents the most probable state of Mercury's interior. However, our results suggest that the existence of an inner core with a radius smaller than 500 km is unlikely. This result concurs with expectations that Mercury's core is at least partially solidified as a consequence of cooling. By including gravitational interaction, we have also found a difference in the optimal moment of inertia ratio found here $\frac{B_m - A_m}{C_m} = (2.19 \pm 0.1) \times 10^{-4}$, compared to the original estimate of $\frac{B_m - A_m}{C_m}$

$= (2.03 \pm 0.04) \times 10^{-4}$ found by Margot *et al.* (2007). While the results of this study provide some insight into Mercury's interior structure, the results show no preferred initial core sulphur concentration and therefore provide little insight into the interior evolution of the planet.

The Messenger and BepiColombo missions that are expected to achieve full orbit in the years 2011 and 2020 respectively are vital to extending our knowledge of Mercury's interior. Both missions are expected to retrieve more accurate and extensive measurements of the libration amplitude, along with an improved and tighter constrained value of the gravitational coefficient C_{22}. Accommodating for these changes in our model will undoubtedly improve the accuracy of results found here. Detailed measurements of Mercury's global magnetic field will provide insights into its origin, and if, as suspected, the magnetic field is sustained by an active dynamo, the measurements of field structure should be able to decipher the approximate core geometry in which the dynamo operates.

Measurements of Love numbers, which describe the reaction of Mercury to tidal forcing are promising to provide relatively detailed estimates of interior geometry (Van Hoolst & Jacobs, 2003). Van Hoolst *et al.* (2003) have shown that the differences in Love numbers associated with different core geometries will be able to place tight constraints on the core size and composition of Mercury. Furthermore, Milani *et al.* (2001) have demonstrated that the BepiColombo mission is expected to provide Love number measurements with a precision of a few percent. Thus, tidal displacement measurements will be able to offer a further mechanism to determine inner core size and sulphur concentration.

It will ultimately be Messenger and BepiColombo that provide the first opportunities to fully understand Mercury's interior. Only after their data are

made available we will be able to trace back into Mercury's past and illuminate the conditions under which the planet accreted.

Bibliography

Anderson, B. J., Acuna, M. H., Korth, H., Purucker, M. E., Johnson, C. L., Slavin, J. A., Solomon, S. C., McNutt Jr, R. L., 2008. The structure of Mercury's magnetic field from MESSENGER's first flyby, *Science.*, **321**, 82.

Anderson, J. D., Colombo, G., Esposito, P. B., Lau, E. L., & Trager, G. B., 1987. The mass, gravity field, and ephemeris of Mercury. *Icarus.*, **71**, 337.

Anderson, J. D., Jurgens, R. F., Lau, E. L., Slade M. A., Schubert, G., 1996. Shape and orientation of Mercury from radar ranging data, *Icarus.*, **124**, 690.

Anderson, O. L., 2003. The three-dimensional phase diagram of iron., *Earth's Core, Dynamics, Structure, Rotation, Geodyn. Ser.*, **31**, pp. 83-103.

Anselmi, A., & Scoon, G. E. N., 2001. BepiColombo, ESA's Mercury Cornerstone mission, *Planet. Space. Sci.*, **49**, 1409-1420.

Balogh, A., & Giampieri, G., 2002. Mercury: The Planet and its orbit, *Rep. Prog. Phys.,* **65**, 529.

Baumgardner, J. R., and Anderson, O. L., 1981. Using the thermal pressure

to compute the physical proporties of terrestrial planets, *Adv. Space Res.*, **1**, 159-176.

Benz, W., Slattery, W. L., Cameron, A. G. W., 1988. Collisional Stripping of Mercury's Mantle, *Icarus.,* **74**, 516-528.

Braginsky, S. I., 1964. Magnetohydrodynamics of the Earth's core, *Geomag. Aeron.,* **4**, pp. 698-711.

Cameron, A. G. W., 1985. The Partial Volatilization of Mercury, *Icarus.,* **64**, 285-294.

Cayley, A., 1859. Tables of the developments of functions in the theory of elliptic motion, *Mem. R. Astron. Soc.*, **29**, 191-306.

Chen, B., Li, J., Hauck, S. A. 2008., Non-ideal liquidus curve in the Fe-S system and Mercury's snowing core, *Geophys. Ress. Lett.,* **35**.

Christensen, U. R., 2006. A deep dynamo generating Mercury's magnetic field, *Nature.*, **444**, 1056-1058.

Colombo, G., 1965. On the rotational period of the planet Mercury, *Nature.*, **208**, 575-577.

Colombo, G., & Shapiro, I. I., 1966. The rotation of the planet Mercury, *Astro. Journal.*, **145**, 296-307.

Crossley, D. J., 1975. The free oscillation equations at the center of the Earth, *Geophys. J. R. astr. Soc.*, **41**, 153-163.

Dahlen, F. A., 1974. On the static deformation of an Earth model with a fluid core, *Geophys. J. R. astro. Soc.,* **36**, 461-485.

Dahlen, F. A., & Tromp, J., 1988. Theoretical global seismology, Princeton University Press, Princeton, NJ.

Danby, J. M. A., 1962. Fundamentals of Celestial Mechanics, The Macmillan Company, New York.

Dehant, V. & Wahr, J. M., 1991. The response of a compressible, non-homogeneous Earth to internal loading: theory, *J. Geomag. Geoelectr.,* **42**, 157-178.

Dumberry, M., 2008. Gravitational torque on the inner core and decadal polar motion, *Geophys. J. Int.,* **172**, 903-920.

Fegley Jr, B., & Cameron, A. G. W., 1987. A vaporization model for iron/silicate fractionation in the Mercury protoplanet, *Earth Planet. Sci. Lett.,* **82**, 207-222.

Fei, Y., Prewitt, C. T., Mao, H., Bertka, C. M., 1995. Structure and density of FeS at high pressure and high temperature and the internal structure of Mars, *Science.*, **268**, 1892-1894.

Forte, A. M. & Peltier, R., 1991. Viscous flow models of global geophysical observables 1. forward problems, *J. Geophys. Res. Lett.,* **22**, 1013-1016.

Gans, R. F., 1972. Viscosity of Earth's Core, *J. Geophys. Res.*, **77**, pp. 360-366.

Goldreich, P., & Peale, S. J., 1966. Spin-orbit coupling in the solar system, *J. Geophys. Res.*, **74**, 2555-2567.

Harder, H., & Schubert, G., 2001. Sulfur in Mercury's core?, *Icarus*, **151**, 118-122.

Heimpel, M.H., Aurnou, J.M., Al-Shamali, F.M., Gomez Perez, N., 2005. A numerical study of dynamo action as a function of spherical shell geometry, *Earth Planet. Sci. Lett.*, **236**, 542-557.

Heimpel, M., & Kabin, K., 2008. Mercury redux, *Nature Geoci.*, **1**, 564-566.

Kaula, W. M., 1966. Theory of Satellite Geodesy: Applications of Satellites to Geodesy. Blaisdell, Waltham, MA.

Kaula, W. M., 1968. An introduction to planetary physics, John Wiley & Sons, Inc., NY.

Lambeck, K., & Pullan, S., 1980. The lunar fossil bulge hypothesis revisited, *Phys. Earth and Planetary Int.*, **22**, 29-35.

Lewis, J. S., 1972. Metal/silicate fractionation in the solar system, *Earth Plan. Sci. Lett.*, **15**, pp. 286-290.

Lewis, J. S., 1988, in Mercury, ed. F. Vilas, C. Chapman, & M. Matthews (Tucson: Univ. of Ariz. Press), 651-666.

Longhi, J., Knittle, E., Holloway, J. R., Waenke, H., 1992. The bulk composition, mineralogy and internal structure of Mars, *Mars.*, edited by Kieffer et al., pp. 184-208, (Tucson: Univ. of Ariz. Press).

Love, J. J., & Bloxham, J., 1994. Electromagnetic coupling and the toroidal magnetic field at the core-mantle boundary, *Geophys. J. Int.*, **117**, 235-236.

Margot, J. L., Peale, S. J., Jurgens, R. F., Slade, M. A., Holin, I. V., 2007. Large longitude libration of Mercury reveals a molten core, *Science*, **316**, 710-714.

Matsuyama, I., & Nimmo, F., 2009. Gravity and tectonic patterns of Mercury: Effect of tidal deformation, spin-orbit resonance, nonzero eccentricity, despinning, and reorientation, *J. Geophys. Res.*, **114**.

Milani, A., Rossi, A., Vokrouhlicky, D., Villani, D., Bonnano, C., 2001. Gravity field and rotation state of Mercury from the BepiColombo Radio Science Experiments, *Planet. Space Sci.*, **49**, 1579-1596.

Ness, N . F., Behannon, K. W., Lepping, R. P., Whang, Y. C., 1974. Magnetic field observations near Mercury: Preliminary results from Mariner 10,

Science., **85**, 151.

Peale, S. J., 1972. Determination of parameters related to the interior of Mercury, *Icarus.*, **17**, pp. 168-173.

Peale, S. J., 1973. Rotation of solid bodies in the solar system, *Rev. Geophys, Space Phys.*, **11**, 767-793.

Peale, S. J., 1976. Does Mercury have a molten core?, *Nature.*, **262**, 765-766.

Peale, S. J., 1981. Measurement accuracies required for the determination of a Mercurian liquid core, *Icarus.*, **48**, 143-145.

Peale, S.J., 1988. Rotational dynamics of Mercury and the state of its core, In: Vilas, F., Chapman, C.R., Matthews, M.S. (Eds.), In: Mercury. Univ. of Arizona Press, Tucson, pp. 461-493.

Peale, S.J., Phillips, R.J., Solomon, S.C., Smith, D.E., Zuber, M.T., 2002. A procedure for determining the nature of Mercury's core, *Meteor. Planet. Sci.*, **37**, 1269-1283.

Peale, S. J., 2005. The free precession and libration of Mercury, *Icarus.*, **178**, 4-18.

Peale, S. J., Yseboodt, M., Margot, J. -L., 2007. Long-period forcing of Mercury's libration in longitude, *Icarus.*, **187**, 365-373.

Pettengill,G. H., & Dyce, R. B., 1965. A radar determination of the rotation of the planet Mercury, *Nature.*, **206**, 1240.

Rambaux, N., Van Hoolst, T., Dehant, V., Bois, E., 2007. Inertial core-mantle coupling and libration of Mercury, *Astron. Astrophys.*, **468**, 711-719.

Rochester, M. G., 1960. Geomagnetic westward drift and irregularities in the Earth's rotation, *Phil. Trans. of the Royal Soc. of London. Series A, Mathematical and Physical Sciences.*, **252**, no 1018, pp 531-555.

Siegfried, R. W., & Solomon, S. C., 1974. Mercury: Internal structure and thermal evolution *Icarus.*, **23**, 192-205.

Solomon, S. C., 1976. Some aspects of core formation in Mercury, *Icarus.*, **28**, 509-521.

Solomon, S. C., 1981,*et al* in Basaltic Volcanism on the Terrestrial Planets, ed. by McGetchin, T. R., Pepin, R. O., Phillips, R. J., (Pergamon, New York), pp. 1129-1233.

Solomon, S. C., and 20 colleagues, 2001. The MESSENGER mission to Mercury: Scientific objectives and implementation, *Planet. Space. Sci.*, **49**, 1445-1465.

Solomon, S. C., McNutt Jr, R. L., Watters, T. R., Lawrence, D. J., Feldman, W. C., Head, J. W., Krimigis, S. M., Murchie, S. L., Phillips, R. J.,

Slavin, J. A., Zuber, M. T., 2008. Return to Mercury: A Global Perspective on MESSENGER's First Mercury Flyby, *Science.*, **321**, 59-62.

Spohn, T., Sohl, F., Wieczerkowski, K., Conzelmann, V., 2001. The interior structure of Mercury: what we know, what we expect from BepiColombo, *Planetary and Space Science*, **49**, 1561-1570.

Stanley, S., Bloxham, J., Hutchison, W.E., Zuber, M.T., 2005. Thin shell dynamo models consistent with Mercury's weak observed magnetic field, *Earth and Planetary Science Letters.*, **234**, 27-38.

Stevenson, D. J., 1980. Applications of liquid state physics to the Earth's core, *Phys. Earth Planet. Inter.,* **22**, pp. 42-52.

Stevenson, D. J., Spohn, T., & Schubert, G., 1983. Magnetism and thermal evolution of the terrestrial planets, *Icarus.*, **54**, 466-489.

Strom, R.G., Trask, N.J., Guest, J.E., 1975. Tectonism and volcanism on Mercury, *J. Geophys. Res.,* **80**, 2478-2507.

Van Hoolst, T., & Jacobs, C., 2003. Mercury's tides and interior structure, *J. Geophys. Res.*, **108**(E11), 5121.

Van Hoolst, T., Sohl, F., Holin, I., Verhoeven, O., Dehant, V., & Spohn, T., 2007. Mercury's interior Structure, Rotation, and Tides, *Space. Sci. Rev.*, **132**, 203-227.

Van Hoolst, T., Rambaux, N., Karatekin, Ö., Dehant, V., Rivoldini, A., 2007. The librations, shape and icy shell of Europa, *Icarus.*, **195**, pp. 386-399.

Wahr, J. M. & de Vries, D., 1989. The possibility of lateral structure inside the core and its implications for nutation and Earth tide observations, *Geophys. J. Int.,* **99**, 511-519.

Wasson, J.T., 1988. The building stones of the planets. *Mercury*, Tucson: Univ. of Ariz. Press.

Watters, T.R., Robinson, M.S., Cook, A.C., 1998. Topography of lobate scarps on Mercury: new constraints on the planet's contraction, *Geology.*, **26**, 991-994.

Weidenschilling, S. J., 1978. Iron/Silicate Fractionation and the Origin of Mercury, *Icarus.*, **35**, 99-111.

Wetherill, G. W. 1988. Accumulation of Mercury from planetesimals, in *Mercury*, ed. F. Vilas, C. Chapman, & M. Matthews (Tucson: Univ. of Ariz. Press), 670-691.

Williams, Q., and Jeanloz, R., 1990. Melting relations in the iron-sulfur system at ultra-high pressure: Implications for the thermal state of the Earth, *J. Geophys. Res.,* **95**,pp. 19299-19310.

Wood, J. A *et al.*, 1981. Basaltic Volcanism on the Terrestrial Planets, ed. by McGetchin, T. R., Pepin, R. O., Phillips, R. J (Pergamon, New York), pp.

634-699.

Yoder, C. F., 1995. Global Earth Physics, A Handbook of Physical Constants, ed. by Ahrens, T. J (*American Geophys. Un*), pp. 1-31.

Zuber, M. T., Aharonson, O., Aurnou, J. M., Cheng, A. F., Hauck II, S. A., Heimpel, M. H., Neumann, G. A., Peale, S. J., Phillips, R. J., Smith, D. E., Solomon, S. C., Stanley, S., 2007. The Geophysics of Mercury: Current status and Anticipated Insights from the MESSENGER Mission, *Space. Sci. Rev.*, **131**, 105-132.

Appendix A

Derivation of $\dot{f}$

From Kepler's second law we know that the Mercury-Sun line sweeps out equal areas A during equal intervals of time, i.e.

$$\frac{dA}{dt} = \frac{r_{orb}^2}{2}\frac{df}{dt} = 0, \tag{A.1}$$

where r_{orb} is the Mercury-Sun distance and f is the true free anomaly which measures the angular position of Mercury with respect to perihelion. Noting that the angular momentum magnitude of Mercury is given by $L = Mvr_{orb}$ with v being the planet's tangential velocity, M is the planet's mass, and substituting for L in (A.1) gives

$$\frac{dA}{dt} = \frac{L}{2M}, \tag{A.2}$$

which can be compared to (A.1) to show that

$$\dot{f} = \frac{df}{dt} = \frac{L}{Mr_{orb}^2}. \tag{A.3}$$

It is possible to rewrite equation (A.3) by integrating (A.2) over one orbital period P an rearranging to get

$$L = \frac{2MA}{P}, \tag{A.4}$$

and also recalling that the area of an ellipse is given by $A = \pi ab$, where the semi-major axis, a and the semi-minor axis, b are related by

$$b^2 = a^2(1 - e^2). \tag{A.5}$$

The above result can be used to express the angular momentum as

$$L = \frac{2M\pi a^2\sqrt{(1 - e^2)}}{P}. \tag{A.6}$$

Upon substitution of equation (A.6) into (A.3), we find

$$\dot{f} = \frac{2\pi a^2\sqrt{(1 - e^2)}}{Pr^2}. \tag{A.7}$$

We also use the geometric equation which relates the distance between Mercury and the Sun to the major and minor axes of the orbit, $r_{orb} = \frac{a(1-e^2)}{1+e\cos f}$ to show

$$\dot{f} = \frac{2\pi}{P}\sqrt{\frac{1}{(1 - e^2)^3}}(1 + e\cos f)^2. \tag{A.8}$$

As a final step we non-dimensionalise our differential equation such that one orbital period P equals 2π such that

$$\dot{f} = \sqrt{\frac{1}{(1 - e^2)^3}}(1 + e\cos f)^2. \tag{A.9}$$

Appendix B

Core Solidification Beyond Eutectic Point

Section 2.3 describes how the inner core obtains an outer layer of eutectic composition as a result of fluid core solidification. The addition of a thin layer of thickness $r_s - r_s^{eut}$ is significant because the inner core as a whole begins to take on a heterogeneous structure. We model this by adding an extra homogeneous layer on top of the pure iron inner core. This effect induces a small change in our expressions for the moments of inertia of the inner core. We ignore the 3.5% density increase that occurs as the fluid core solidifies on to the inner core. For this reason, the density of this additional homogeneous layer is assumed to be the same as that of the outer core after the eutectic limit has been reached,

$$\rho_s^{eut} = \left(\frac{\chi_{FeS}^{eut}}{\rho_{FeS}^{liquid}} + \frac{1 - \chi_{FeS}^{eut}}{\rho_{Fe}^{liquid}} \right)^{-1}. \tag{B.1}$$

This expression is analogous with (2.5) but the composition χ_{FeS} has been replaced with the eutectic composition χ_{FeS}^{eut}. The mass of the inner core

becomes

$$M_s = \frac{4\pi}{3}\left[\rho_s(r_s^{eut})^3 + \rho_s^{eut}\big(r_s^3 - (r_s^{eut})^3\big)\right] \tag{B.2}$$

and the moments of inertia take on the form

$$B_s - A_s = \frac{8\pi}{15}\epsilon_i\left[\rho_s(r_s^{eut})^5 + \rho_s^{eut}\big(r_s^5 - (r_s^{eut})^5\big)\right] \tag{B.3}$$

$$C_s = \frac{8\pi}{15}\left[\rho_s(r_s^{eut})^5 + \rho_s^{eut}\big(r_s^5 - (r_s^{eut})^5\big)\right]. \tag{B.4}$$

The subtle changes in inertia have a small effect on the ellipticity of equipotential surfaces in the mantle ϵ_m and at the CMB ϵ_f. These adjustments are manifested throughout all of the parameters that require the use of inertia in their definition. In light of these changes, the ellipticity of the mantle and the core-mantle boundary can be revised to give

$$\epsilon_f = \frac{10\bar{\rho}C_{22} - \Delta\gamma_m\left[1 - \left(\frac{r_f}{r_e}\right)^5\right]\left[\rho_m + k_m(\rho_s - \rho_s^{eut})\left(\frac{r_s^{eut}}{r_e}\right)^5\right]}{\rho_s^{eut}\left(\frac{r_f}{r_e}\right)^5 + (\rho_s - \rho_s^{eut})\left(\frac{r_s^{eut}}{r_e}\right)^5\left[k_f + k_m\left(\frac{r_f}{r_e}\right)^5\right]} \tag{B.5}$$

and

$$\epsilon_m = \frac{10\bar{\rho}C_{22}\left(\frac{r_f}{r_e}\right)^5 - \Delta\gamma_m\left[1 - \left(\frac{r_f}{r_e}\right)^5\right]\left[(\rho_s^{eut} - \rho_m)\left(\frac{r_f}{r_e}\right)^5 + k_f(\rho_s - \rho_s^{eut})\left(\frac{r_s^{eut}}{r_e}\right)^5\right]}{\rho_s^{eut}\left(\frac{r_f}{r_e}\right)^5 + (\rho_s - \rho_s^{eut})\left(\frac{r_s^{eut}}{r_e}\right)^5\left[k_f + k_m\left(\frac{r_f}{r_e}\right)^5\right]} \tag{B.6}$$

respectively.

The coupling constant $\overline{\Gamma}$ must also undergo a transformation. From (B.3) we note that $\frac{B_s - A_s}{C_s} = \epsilon_i$. Substituting into the torque equation we find

$$\overline{\Gamma} = \frac{4\pi G}{5}\left|\overline{\rho\epsilon} + \rho_f\epsilon_i\right|\left|(B_s - A_s) - (B_s' - A_s')\right| \tag{B.7}$$

$$= \left(\frac{4\pi G}{5}\right)\big(C_s - \tilde{C}_s\big)\epsilon_i\big((\rho_f - \rho_m)\epsilon_f + \rho_m\epsilon_m\big), \tag{B.8}$$

where $\tilde{C}_s = \frac{8\pi}{15}\rho_s^{eut} r_s^5$. The coupling parameter is constant beyond the eutectic radius, and in order to prove this is the case, we expand $C_s - \tilde{C}_s$,

$$C_s - \tilde{C}_s = \frac{8\pi}{15}\left[\rho_s (r_s^{eut})^5 - \rho_s^{eut}(r_s^{eut})^5\right], \tag{B.9}$$

which is constant. In order for $\bar{\Gamma}$ to be constant for $r \geq r_s$, ϵ_m, ϵ_f and ϵ_i must also be constant for the same range of radii. The fact that equations (B.5) and (B.6) do not depend on r_s proves that ϵ_m, ϵ_f are indeed constant for $r \geq r_s$ (also see figure 5.5). This is also the case for $\epsilon_i = k_m\epsilon_m + k_f\epsilon_f$, since k_m and k_f are also constant for inner core radii larger than the eutectic radius (see figure 5.6). It should be noted that this would not be the case for $\bar{\Gamma}$ if we accounted for the 3.5% density difference due to the phase change since the expression would be a function of inner core radius.

Appendix C

Deformation of Material Surfaces in the Core

The lateral density anomalies associated with mantle and crustal structure lead to global variations in the gravitational potential. We express the gravitational potential Φ everywhere inside Mercury as a sum of its radial component $\Phi_0(r)$ and its deviation from spherical symmetry in terms of spherical harmonic functions Y_l^m (e.g. Dahlen & Tromp, 1988) with coefficients $\delta\Phi_l^m(r)$. The radial component $\Phi_0(r)$ is related to the reference, spherically symmetric state which is in hydrostatic equilibrium, as defined by equations (3.1) and (3.2). We thus write

$$\Phi = \Phi_0(r) + \sum_l \sum_m \delta\Phi_l^m(r) Y_l^m. \tag{C.1}$$

To simplify the notation, from this point onward we drop the indices l and m on the spherical harmonic coefficients. Thus, $\delta\Phi \equiv \delta\Phi_l^m$, though it has to be understood that $\delta\Phi$ is the coefficient for one particular degree l and order m. This convention applies to the deviation of any quantity X; the notation δX

represents one spherical harmonic coefficient of X.

Each coefficient $\delta\Phi$ can be separated into five different contributions,

$$\delta\Phi = \delta\Phi_M + \delta\Phi_{TM} + \delta\Phi_I + \delta\Phi_{TI} + \delta\Phi_F \tag{C.2}$$

The first part, $\delta\Phi_M$, represents the gravitational potential from density anomalies in the mantle. At Mercury's CMB, it is related to density anomalies by (e.g. Kaula, 1968)

$$\delta\Phi_M(r_f) = -\frac{4\pi G}{2l+1} r_f^l \int_{r_f}^{r_e} \frac{\delta\rho}{a^{l-1}} da, \tag{C.3}$$

where $\delta\rho$ is the spherical harmonic coefficient of the same degree and order expressing density variations from spherical symmetry. The part $\delta\Phi_{TM}$ represents the contribution from topography at density discontinuities in the mantle. This includes Mercury's surface and the CMB. At Mercury's CMB (e.g. Kaula, 1968),

$$\delta\Phi_{TM}(r_f) = \frac{4\pi G}{2l+1} \sum_j [\rho_0(d_j)]_-^+ \frac{r_f^l}{d_j^{l-1}} \Delta h(d_j), \tag{C.4}$$

where $\Delta h(d_j)$ is the spherical harmonic coefficient of the displacement from the j-th density discontinuity with radius d_j. The notation $[X(d_j)]_-^+$ is used to represent the discontinuity in a quantity X at $r = d_j$. Just below the CMB, $\delta\Phi_M$ and $\delta\Phi_{TM}$ are externally imposed potentials and they must satisfy Laplace's equation. Therefore, they must be harmonic functions, and for $r < r_f$

$$\delta\Phi_M(r) = \delta\Phi_M(r_f)\left(\frac{r}{r_f}\right)^l, \tag{C.5}$$

and similarly for $\delta\Phi_{TM}$.

The part $\delta\Phi_I$ represents the contribution from density anomalies within

the inner core due to non-hydrostatic processes, whereas $\delta\Phi_{TI}$ is that from topography at the inner core boundary (ICB) and any additional density discontinuities that may exist within the inner core, also due to non-hydrostatic processes. At the ICB,

$$\delta\Phi_I(r_s) = -\frac{4\pi G}{2l+1}\frac{1}{r_s^{l+1}}\int_0^{r_s}\delta\rho\; a^{l+2}da. \tag{C.6}$$

$$\delta\Phi_{TI}(r_s) = \frac{4\pi G}{2l+1}\sum_j[\rho_0(d_j)]_-^+\frac{d_j^{l+2}}{r_i^{l+1}}\Delta h(d_j). \tag{C.7}$$

However, we assume that deformation in the whole core is caused only by a response to the gravitational forcing from the mantle, and the terms due to non-hydrostatic processes become $\delta\Phi_I = \delta\Phi_{TI} = 0$. These results are consistent with the assumption that the inner core is in hydrostatic equilibrium, at least on timescales shorter than the expected timescale of characteristic changes in $\delta\Phi_M$ and $\delta\Phi_{TM}$.

In response to $\delta\Phi_M$ and $\delta\Phi_{TM}$ the fluid core must deform in a similar manner to the inner core so that the surfaces of constant density within the whole core remain coincident with surfaces of constant gravitational potential and hydrostatic equilibrium is maintained. Density anomalies result from the deformation of the spherically symmetric reference state. The contribution to the global gravitational potential in response to these anomalies is the part denoted by $\delta\Phi_F$ in (C.2), and includes the contributions from hydrostatic deformation of the outer and inner cores. If we note the displacement of surfaces of constant gravitational potential in the core as δu, then the change in density in the core $\delta\rho$ is

$$\delta\rho = -\delta u\frac{\partial\rho_0}{\partial r}. \tag{C.8}$$

The potential $\delta\Phi_F$ is caused by this density perturbation and inside the whole

core the two are related through Poisson's equation

$$\nabla^2 \delta\Phi_F = 4\pi G \delta\rho. \tag{C.9}$$

In the mantle, $\delta\Phi_F$ satisfies Laplace's equation, so

$$\delta\Phi_F(r) = \delta\Phi_F(r_f)\left(\frac{r_f}{r}\right)^{(l+1)}, \quad \text{for} \;\; r > r_f. \tag{C.10}$$

Since $\delta\Phi_F$ is a consequence of an externally imposed potential, it must be related to it and we now proceed to determine this relationship.

The static equilibrium in the core is governed by the linear first order perturbations in the hydrostatic balance,

$$\mathbf{0} = -\nabla\delta p - \rho_0 \nabla(\delta\Phi_F + \delta\Phi_E) - \delta\rho \; g_0 \hat{\mathbf{r}}, \tag{C.11}$$

where δp is the change in pressure and $\delta\Phi_E$ represents all the potentials external to the outer core, i.e. $\delta\Phi_E = \delta\Phi_M + \delta\Phi_{TM}$. Since $\delta\Phi_E$ must satisfy Laplace's equation in the fluid core, we can add this contribution to equation (C.9) and solve for the equivalent problem

$$\nabla^2 \delta\Phi = 4\pi G \delta\rho, \tag{C.12}$$

$$\mathbf{0} = -\nabla\delta p - \rho_0 \nabla\delta\Phi - \delta\rho \; g_0 \hat{\mathbf{r}}, \tag{C.13}$$

where $\delta\Phi$ is the total gravitational potential in the fluid core, as specified by (C.2) (with $\delta\Phi_I = \delta\Phi_{TI} = 0$). By taking the transverse component of (C.13), it follows that

$$\delta p = -\rho_0 \delta\Phi. \tag{C.14}$$

Taking the radial component of (C.13) reveals

$$\frac{\partial \delta p}{\partial r} = -\rho_0 \frac{\partial \delta \Phi}{\partial r} + \delta u \frac{\partial \rho_0}{\partial r} g_0, \tag{C.15}$$

where the result of (C.8) has been used in (C.15). A further substitution of the result $\delta p = -\rho_0 \delta \Phi$ into equation (C.15) reveals

$$\delta u = -\frac{\delta \Phi}{g_0}. \tag{C.16}$$

Equations (C.8), (C.14) and (C.16) represent the coherent displacement of surfaces of constant density, gravitational potential and pressure that characterises hydrostatic equilibrium.

By combining (C.8), (C.12) and (C.16), $\delta\Phi$ in the core must respect the differential equation

$$\nabla^2 \delta \Phi = \frac{4\pi G}{g_0} \frac{\partial \rho_0}{\partial r} \delta \Phi, \tag{C.17}$$

or in its expanded form (Dahlen, 1974),

$$\frac{\partial^2 \delta \Phi}{\partial r^2} + \frac{2}{r} \frac{\partial \delta \Phi}{\partial r} - \left[\frac{l(l+1)}{r^2} + \frac{4\pi G}{g_0} \frac{\partial \rho_0}{\partial r} \right] \delta \Phi = 0. \tag{C.18}$$

Solutions to (C.18) can be found by specifying four boundary conditions on $\delta\Phi$. The two conditions at the ICB,

$$[\delta \Phi]^+_- = 0, \tag{C.19}$$

$$\left[\frac{\partial \delta \Phi}{\partial r} + 4\pi G \rho_0 \Delta h \right]^+_- = 0, \tag{C.20}$$

represent continuity of gravitational potential and gravitational flux across the ICB, respectively. The same conditions apply at the CMB, but can be

constructed into a single condition,

$$\frac{\partial \delta\Phi}{\partial r} + \frac{l+1}{r_f}\delta\Phi = \frac{2l+1}{r_f}\big(\delta\Phi_M(r_f) + \delta\Phi_{TM}(r_f)\big). \tag{C.21}$$

The final condition is one at the origin, and can be found by expanding $\delta\Phi$ in a power series (e.g. Crossley, 1975). Exact solutions to (C.18) can be constructed by a numerical integration. For the special case where $\frac{\partial \rho_0}{\partial r} = 0$, and so for the models used in our study, an analytical solution exists, given by

$$\delta\Phi = F g_0(r) r_f \left(\frac{r}{r_f}\right)^{l-1}. \tag{C.22}$$

The constant F can be determined from (C.21) and is

$$F = \frac{2l+1}{r_f}\frac{\delta\Phi_M + \delta\Phi_{TM}}{2(l-1)g_f + 4\pi G\rho_f r_f}. \tag{C.23}$$

This is a useful result because we can use it to calculate the ellipticity of material surfaces inside the core ϵ_i. Temporarily reinstating the indices l and m and substituting (C.22) into (C.16) gives

$$\delta u_l^m = -F r_f \left(\frac{r}{r_f}\right)^{l-1}. \tag{C.24}$$

If we relate the displacement of equipotential surfaces δu_l^m to the core ellipticity ϵ_l^m through the expression $\delta u_l^m = r\epsilon_l^m$, we can rewrite (C.24) to show

$$\epsilon_l^m = -F\left(\frac{r}{r_f}\right)^{l-2}. \tag{C.25}$$

Solving for the $l = 2$, $m = 2$ component reveals

$$\epsilon_i = \epsilon_2^2 = -F = -\frac{5}{r_f}\left(\frac{\delta\Phi_M + \delta\Phi_{TM}}{2g_f + 4\pi G\rho_f r_f}\right), \tag{C.26}$$

which can be used to calculate the shape of equipotential surfaces in the entire core. Thus, the ellipticity of equipotential and material surfaces are constant throughout the core. Note that for our interior models of Mercury, with homogeneous mantle density ρ_m, the term $\delta\Phi_M = 0$. Hence, the only contribution to non-spherical gravity comes from $\delta\Phi_{TM}$ and the elliptical geometries of the core and CMB.